

FORSCHUNGSZENTRUM KARLSRUHE

T e c h n i k u n d U m w e l t

Wissenschaftliche Berichte

FZKA 6019

**CORSIKA: A Monte Carlo Code to
Simulate Extensive Air Showers**

D. Heck¹, J. Knapp², J.N. Capdevielle³, G. Schatz¹, T. Thouw¹

¹ Institut für Kernphysik, Forschungszentrum Karlsruhe, D 76021 Karlsruhe

² Institut für Experimentelle Kernphysik, Universität Karlsruhe, D 76021 Karlsruhe

³ Physique Corpusculaire et Cosmologie, Collège de France, F 75231 Paris Cedex 05,
France

Forschungszentrum Karlsruhe GmbH, Karlsruhe

1998

Copyright Notice

Copyright and any other appropriate legal protection of these computer programs and associated documentation reserved in all countries of the world.

These programs or documentation may not be reproduced by any method without prior written consent of FORSCHUNGSZENTRUM KARLSRUHE or its delegate.

FORSCHUNGSZENTRUM KARLSRUHE welcomes comments concerning the CORSIKA code but undertakes no obligation for maintenance of the programs, nor responsibility for their correctness, and accepts no liability whatsoever resulting from the use of its programs.

Trademark notice: All trademarks appearing in this report are acknowledged as such.

Abstract

CORSIKA: A Monte Carlo Code to Simulate Extensive Air Showers

CORSIKA is a program for detailed simulation of extensive air showers initiated by high energy cosmic ray particles. Protons, light nuclei up to iron, photons, and many other particles may be treated as primaries. The particles are tracked through the atmosphere until they undergo reactions with the air nuclei or - in the case of instable secondaries - decay. The hadronic interactions at high energies may be described by five reaction models alternatively: The VENUS, QGSJET, and DPMJET models are based on the Gribov-Regge theory, while SIBYLL is a minijet model. HDPM is a phenomenological generator and adjusted to experimental data wherever possible. Hadronic interactions at lower energies are described either by the more sophisticated GHEISHA interaction routines or the rather simple ISOBAR model. In particle decays all decay branches down to the 1% level are taken into account. For electromagnetic interactions the shower program EGS4 or the analytical NKG formulas may be used. Options for the generation of Cherenkov radiation and neutrinos exist.

Zusammenfassung

CORSIKA: Ein Monte Carlo Programm zur Luftschauersimulation

CORSIKA ist ein Programm zur detaillierten Simulation von ausgedehnten Luftschauern, die durch hochenergetische kosmische Strahlung ausgelöst werden. Als Primärteilchen können Protonen, leichte Kerne bis Eisen, Photonen und viele andere Teilchen behandelt werden. Die Teilchen werden durch die Atmosphäre verfolgt, bis sie mit den Kernen der Luft reagieren oder - im Falle von instabilen Sekundärteilchen - zerfallen. Die hadronischen Wechselwirkungen bei hohen Energien können wahlweise von fünf verschiedenen Reaktionsmodellen beschrieben werden: Die Modelle VENUS, QGSJET und DPMJET basieren auf der Gribov-Regge Theorie, während SIBYLL ein Mini-Jet Modell ist. HDPM ist ein phänomenologischer Generator und angepaßt an experimentellen Daten, wo immer das möglich ist. Hadronische Wechselwirkungen bei niedrigeren Energien werden entweder durch die detaillierten GHEISHA Wechselwirkungsroutinen oder durch das ziemlich einfache Isobaren-Modell beschrieben. Bei Teilchenzerfällen werden alle Zerfallskanäle bis herab zu 1% Häufigkeit berücksichtigt. Elektromagnetische Prozesse können mit dem Schauerprogramm EGS4 oder mit den analytischen NKG-Formeln behandelt werden. Es gibt Optionen für die Erzeugung von Cherenkov-Strahlung und von Neutrinos.

Contents

1	Introduction	1
2	Program frame	5
2.1	Control and run	5
2.2	Particles	5
2.3	Coordinate system	6
2.4	Atmosphere	6
2.5	Random number generator	8
3	Particle tracking	9
3.1	Ionization energy loss	9
3.2	Coulomb multiple scattering	10
3.2.1	Molière scattering	11
3.2.2	Plural Coulomb scattering	12
3.2.3	Gaussian approximation	12
3.3	Deflection in the Earth's magnetic field	13
3.4	Time of flight	13
3.5	Longitudinal development	14
3.6	Thin sampling	14
4	Mean free path	17
4.1	Muons	17
4.2	Nucleons and nuclei	19
4.2.1	Nucleon-air cross section at high energies	20
4.2.2	Nucleon-air cross section at low energies	21
4.2.3	Nucleus-nucleus cross section	21
4.3	Pions and kaons	24
4.4	Other hadrons and resonances	25
4.5	Neutrinos	27
5	Hadronic interactions	29
5.1	Strong interactions at high energies	29
5.1.1	VENUS	30

5.1.2	QGSJET	31
5.1.3	DPMJET	32
5.1.4	SIBYLL	32
5.1.5	HDPM	33
5.2	Strong interactions at low energies	33
5.2.1	GHEISHA	33
5.2.2	ISOBAR	34
5.3	Nuclear fragmentation	35
6	Particle decays	37
6.1	π^0 decays	37
6.2	π^\pm decay	38
6.3	Muon decay	38
6.4	Kaon decays	39
6.5	η decays	42
6.6	Strange baryon decays	42
6.7	Resonance decays	43
7	Electromagnetic interactions	45
7.1	Muonic interactions	45
7.1.1	Muonic bremsstrahlung	45
7.1.2	Muonic e^+e^- -pair production	46
7.2	Electromagnetic subshowers	47
7.2.1	Electron gamma shower program EGS4	48
7.2.2	Nishimura-Kamata-Greisen option	51
7.3	Cherenkov radiation	54
8	Outlook	57
A	Atmospheric parameters	59
B	Muon range for horizontal showers	63
C	Default cross sections	65
C.1	Nucleon-nucleon cross sections	65
C.2	Pion-nucleon and kaon-nucleon cross sections	66
D	HDPM	67
D.1	Nucleon-nucleon interactions	68
D.2	Nucleon-nucleus interactions	78
D.3	Pion-nucleus and kaon-nucleus interactions	79
D.4	Nucleus-nucleus interactions	79
	Acknowledgements	81

Chapter 1

Introduction

Analyzing experimental data on Extensive Air Showers (EAS) or planning corresponding experiments requires a detailed theoretical modelling of the cascade which develops when a high energy primary particle enters the atmosphere. This can only be achieved by detailed Monte Carlo calculations taking into account all knowledge of high energy strong and electromagnetic interactions. Therefore, a number of computer programs has been written to simulate the development of EAS in the atmosphere and a considerable number of publications exists discussing the results of such calculations. A common feature of all these publications is that it is difficult, if not impossible, to ascertain in detail which assumptions have been made in the programs for the interaction models, which approximations have been employed to reduce computer time, how experimental data have been converted into unmeasured quantities required in the calculations (such as nucleus-nucleus cross sections, e.g.) etc. This is the more embarrassing, since our knowledge of high energy interactions – though much better today than fifteen years ago – is still incomplete in important features. This makes results from different groups difficult to compare, to say the least. In addition, the relevant programs are of a considerable size which – as experience shows – makes programming errors almost unavoidable, in spite of all undoubted efforts of the authors. We therefore encourage the groups engaged in this work to make their programs available to (and, hence, checkable by) other colleagues. This procedure has been adopted in high energy physics and has proved to be very successful. It is in the spirit of these remarks that we want to describe in this report the physics underlying the CORSIKA program.

CORSIKA (**CO**smic **R**ay **SI**mulations for **KA**scade) is a detailed Monte Carlo program to study the evolution of EAS in the atmosphere initiated by photons, protons, nuclei, or any other particle. It was originally developed to perform simulations for the KASCADE experiment [1, 2] at Karlsruhe and has been refined over the past years. CORSIKA meanwhile has developed into a tool that is used by many groups. Its applications range from Cherenkov telescope experiments ($E_0 \approx 10^{12}$ eV) up to the highest energies observed ($E_0 > 10^{20}$ eV). The development of CORSIKA is guided by the idea to predict not only correct average values of observables with this

EAS simulation code, but also to reproduce the correct fluctuations around the average value. Therefore, where available, we include all known processes which might have a noticeable influence on the observable quantities of EAS to create a reference program that treats all processes to the present state of our knowledge. This concerns the transport of particles through the atmosphere as well as their interactions with air as a target. All secondary particles are tracked explicitly along their trajectories and their parameters are stored on tape when reaching an observation level. This allows a detailed analysis of all features of simulated showers.

The CORSIKA code has originally been developed on the basis of three well established program systems. The first was written in the 1970s by Grieder [3]. Its general program structure has been adopted in CORSIKA and its ISOBAR routines, a simple hadronic interaction model, may be used as a quick alternative for the hadronic interactions at low energies. The second part, the interaction generator HDPM, was developed by Capdevielle [4] inspired by the Dual Parton Model [5]. It describes the hadronic interactions of protons at high energies in good agreement with the measured collider data. The third program deals with the simulation of the electromagnetic part of an air shower. We incorporated the code EGS4 [6] used successfully in the detector simulation of particle physics experiments. It was slightly modified to the requirements of air shower simulations. These programs were merged together and formed the first version of CORSIKA in 1989.

Basing on this primordial program many extensions and improvements have been performed since that time. The most serious problem of EAS simulation programs is the extrapolation of hadronic interaction to higher energies and into rapidity ranges which are not covered by experimental data. The extreme forward direction is not accessible by present collider experiments, rather the particles vanish undetected in the beam pipe. But just these particles are of highest importance in the development of EAS, as they are the most energetic secondary particles, which bring the largest energy fraction of each collision deep into the atmosphere. Also, $p\bar{p}$ -colliders are, and will be, limited in their maximum attainable energy to values much lower than those found in cosmic rays. Therefore one has to rely on extrapolations based on theoretical models. To study the systematics of such models, we have made five different hadronic interaction models available in CORSIKA to simulate the hadronic interactions at high energies: VENUS [7], QGSJET [8], and DPMJET [9] which describe the inelastic hadronic interactions in the theoretically well founded manner of the Gribov-Regge formalism, and the minijet model SIBYLL [10, 11]. These four models give us an alternative to the phenomenological HDPM generator. Also the GHEISHA routines [12] have been coupled which represent a more sophisticated replacement of the ISOBAR model for the treatment of low energy hadronic interactions. With the advent of the announced successor of VENUS [13] we plan to make it also available within CORSIKA.

The fragmentation of nuclei in a collision may be treated in various ways, including two options of particle evaporation from the residual nucleus. The photoproduction of muon pairs and hadrons is incorporated into EGS4 [6]. This allows the calculation

of the muon content of photon induced showers. An alternative way of treating the electromagnetic component is to use the improved and adapted form [14, 15, 16] of the analytic NKG formula for each electron or photon produced in the hadronic cascade. It allows to study the longitudinal development of the electromagnetic cascade and the electron density at particular coordinates at the observation level. This option enables a fast but less accurate simulation of hadronic showers.

Further options treat the detailed longitudinal development of various particle species within an air shower, the production of electron and muon neutrinos and anti-neutrinos, and the production of Cherenkov radiation. The elemental composition of the atmosphere is included as well as the density variation with altitude for several seasonal days. For nearly horizontal showers various zenith angle dependent density profiles are provided which take into account the influence of the Earth's curvature in our flat atmospheric model.

With this program many calculations have been performed with p , α , O , Fe and γ primaries in an energy range of $10^{11} \text{ eV} \leq E_0 \leq 10^{16} \text{ eV}$ by the KASCADE group. Also various laboratories around the world use CORSIKA to interpret and understand their cosmic ray experiments [17, 18]. Particle numbers for electrons, muons, and hadrons, their lateral and energy distributions, arrival times, and many other features have been evaluated from the simulations and compared with experimental data, where available. The agreement gives us confidence to have with CORSIKA a useful and flexible tool to study cosmic rays and their secondaries at high primary energies. We invite all colleagues interested in EAS simulation to propose improvements, point out errors, or bring forward reservations concerning assumptions or approximations which we have made.

The scope of this report is a description of the physical basis and the parametrizations actually used in CORSIKA and to show its capabilities and limitations. The program is in permanent modification by improvements, additions, and further details [19, 20]. This report refers to the actual version¹ and overrides the older description [21]. Most recent changes, however, were shown to have minor effects on the global features of simulated showers.

Additionally there exists a user's guide [22], describing how to install the program and how to handle input and outputs. This technical report is permanently updated and available² together with the complete program package from the anonymous ftp installed at the server `ftp-ik3.fzk.de`. This package includes the source codes of CORSIKA and all interaction programs, the necessary datasets, an input example, and the user's guide. It enables the user to setup the program with the desired options and to run it with suitable parameters. Information on CORSIKA may be found also in the world wide web at page `http://www-ik3.fzk.de/~heck/corsika/`.

¹Version 5.60 released in Dec. 1997

²Requests for ftp-access should be directed to `<heck@ik3.fzk.de>` or `<knapp@ik1.fzk.de>` by e-mail.

Chapter 2

Program frame

2.1 Control and run

At the beginning of the calculation a variety of parameters can be chosen to control the simulation. The primary particle type has to be defined, and its energy can be prechosen or selected at random in a particular energy range with a given slope of the energy spectrum. This allows a realistic simulation of the shower rate falling steeply with rising energy. The primary angle of incidence may be defined to a fixed value or picked at random within an angular range in a manner giving the experimentally observable intensity of an equal particle flux from all directions of the sky penetrating through a horizontal detector area [23]. The atmospheric parameters may be selected to study the influence of the seasons. Up to 10 observation levels can be defined and data on all particles penetrating these levels are recorded as long as the energy exceeds a cut-off, specified for hadrons, muons, electrons, or photons separately. Several flags select and control the hadronic interaction models at high energies and the respective cross sections, one flag selects the low energy hadronic interaction model. Various possibilities exist to simulate the fragmentation of the primary nucleus, and two flags switch on or off the two options for the simulation of electromagnetic cascades. Using the ‘thin sampling’ option the thinning level may be specified. All these controls, also on the printing of various lists and tables, are described extensively in Ref. [22].

2.2 Particles

The CORSIKA program recognizes 50 elementary particles. These are γ , e^\pm , μ^\pm , π^0 , π^\pm , K^\pm , $K_{S/L}^0$, η , the baryons p , n , Λ , Σ^\pm , Σ^0 , Ξ^0 , Ξ^- , Ω^- , the corresponding anti-baryons, the resonance states ρ^\pm , ρ^0 , $K^{*\pm}$, K^{*0} , \bar{K}^{*0} , Δ^{++} , Δ^+ , Δ^0 , Δ^- , and the corresponding anti-baryonic resonances. Optionally the neutrinos ν_e and ν_μ and anti-neutrinos $\bar{\nu}_e$ and $\bar{\nu}_\mu$ resulting from π , K , and μ decay may be generated explicitly. In addition nuclei up to $A = 56$ can be treated. Within the program they are identified

by their numbers of protons and neutrons. All these particles can be tracked through the atmosphere, are able to interact, annihilate or decay, and produce secondary particles. They are fully defined in the program by their particle identification, the Lorentz factor, the zenith and azimuthal angle of the trajectory, the time since the first interaction of the primary, and the three spatial coordinates x , y , and z . The number of inelastic hadronic reactions or decays which the parent particles have suffered is protocoled as the generation of a particle. The particle masses and charge states are stored in an array for fast access during the calculations. Particle identifiers and masses of elementary particles are taken from the GEANT3 detector simulation code [24] with extensions for 4 neutrino species and resonance states; the resonance masses correspond with Ref. [25]. The nuclear masses are taken as the sum of the constituent nucleon masses neglecting binding energies. If nuclear binding effects should be regarded, we provide as an alternative for nuclei with $Z < 15$ the isotopic masses from the mass table of Ref. [26] with corrections for the electron masses and for other nuclear masses a calculation according to the Bethe-Weizsäcker formula. Projectile nuclei are assumed to be completely stripped, i.e. their charge state q is set equal to their atomic number Z .

2.3 Coordinate system

The coordinates in CORSIKA are defined with respect to a Cartesian coordinate system with the positive x -axis pointing to the magnetic north, the positive y -axis to the west, and the z -axis upwards. The origin is located at sea level. This definition is necessary, because the Earth's magnetic field is taken into account. By default it is implemented for the location of Karlsruhe (49° N, 8° E) as described in section 3.3. The zenith angle θ of a particle trajectory is measured between the particle momentum vector and the negative z -axis, and the azimuthal angle ϕ between the positive x -axis and the x - y -component of the particle momentum vector (i.e. with respect to north) proceeding counterclockwise.

2.4 Atmosphere

The atmosphere adopted consists of N_2 , O_2 , and Ar with the volume fractions of 78.1%, 21.0%, and 0.9% [27]. The density variation of the atmosphere with altitude is modeled by 5 layers. The boundary of the atmosphere in this model is defined at the height H . In the lower four of them the density follows an exponential dependence on the altitude leading to a relation between the mass overburden $T(h)$ of the atmosphere and the height h of the form

$$T(h) = a_i + b_i e^{-h/c_i} \quad i = 1, \dots, 4 \quad . \quad (2.1)$$

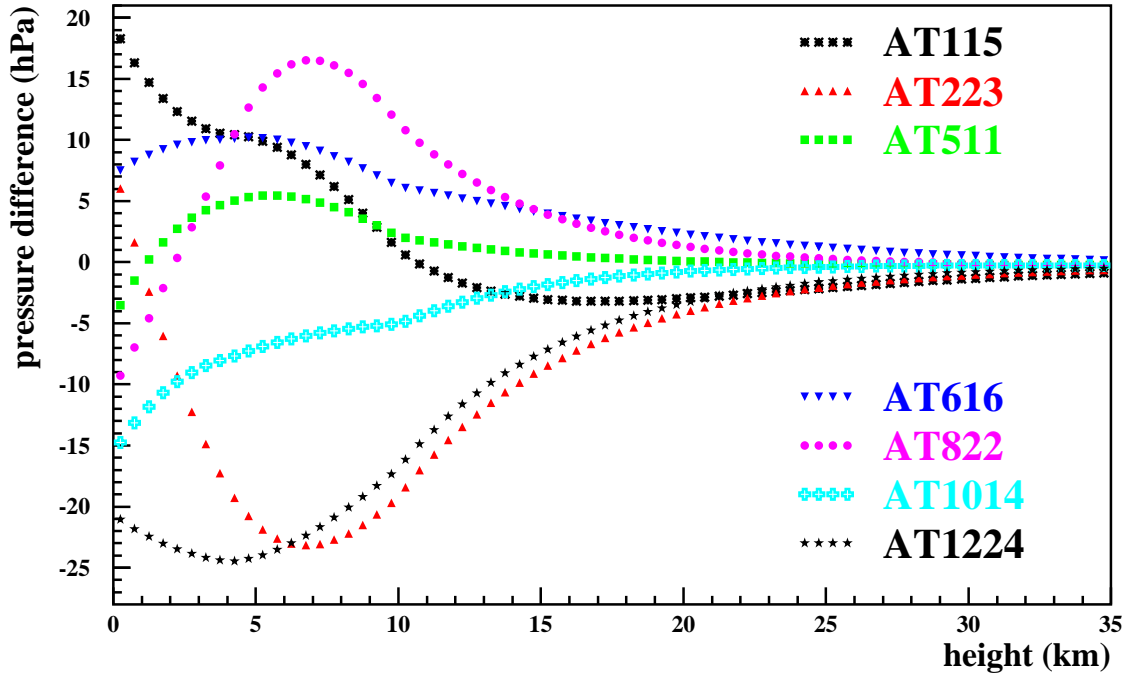


Figure 2.1: Pressure difference of the atmosphere above Stuttgart (Germany) at 7 days distributed over the year 1993 relative to U.S. standard atmosphere.

In the fifth layer the mass overburden decreases linearly with height

$$T(h) = a_5 - b_5 \frac{h}{c_5} \quad . \quad (2.2)$$

where the mass overburden $T(h)$ vanishes, which is at $h = 112.8 \text{ km}$. The parameters a_i , b_i , and c_i are selected in a manner that the function $T(h)$ is continuous at the layer boundaries and can be differentiated continuously. Various atmospheres are foreseen: U.S. standard atmosphere parametrized according to J. Linsley [28], 7 typical atmospheres as measured above Stuttgart (about 60 km away from Karlsruhe) at various days of 1993, transmitted by Deutscher Wetterdienst Offenbach and parametrized according Ref. [29]. Out of a large ensemble of measured atmospheres these 7 sets have been selected such that characteristic seasonal differences show up. The parameter values of the available atmospheres are listed in Tables A.1 to A.8. Fig. 2.1 shows the pressure difference of the 7 atmospheres relative to the U.S. standard atmosphere. Therefore also the pressure at ground level varies from parameter set to parameter set, as listed in Table A.9.

In CORSIKA always a flat atmosphere is adopted. In the simulation of nearly horizontal showers with $\theta \geq 75^\circ$ the influence of the curvature of the Earth's surface

is no longer negligible. To avoid the lengthy calculations in a spherical coordinate system, optionally the analytical description of the atmosphere may be replaced by tabulated mass overburden distributions, calculated for that angle. Thus we simulate those nearly horizontal showers with $\theta = 0$, but with an atmospheric profile which is present along the axis of a nearly horizontal shower.

The passage of the primary particle through the atmosphere starts at the upper border of the atmospheric model. From this starting point the place of the first interaction is calculated. The height and the target nucleus of this interaction are selected at random. Optionally both selections may be fixed by input values. The coordinates of the point of first interaction are set to $(0, 0, z_0)$. At each observation level the x and y coordinates are shifted such that the shower axis retains the coordinates $(0, 0, z_{obs})$. This is done to facilitate later analysis.

2.5 Random number generator

The Monte Carlo method is essentially based on random numbers and, hence, a random number generator that meets the requirements of the today's increasingly long and complex calculations is indispensable. CORSIKA is operated with the random number generator RANMAR [30] in the version as implemented in the CERN program library [31] which represents the state of the art in computational physics. It is a pseudo random number generator delivering uniformly distributed numbers. It offers the possibility to generate simultaneously up to $9 \cdot 10^8$ independent sequences with a sequence length of $\approx 2 \cdot 10^{44}$ each. The generator is written in standard FORTRAN and, thus, portable to all types of computers where bit-identical results are obtained. It satisfies very stringent tests on randomness and uniformity and it is sufficiently fast.

Chapter 3

Particle tracking

For propagating particles between two interaction points their space and time coordinates as well as their energy have to be updated. For electrons and photons this is done in EGS4 as described in Ref. [6] and section 7.2.1. Charged particles lose energy by ionization whereas neutral particles proceed without energy loss. Because of the large penetration depth of μ^\pm a deflection due to multiple Coulomb scattering is taken into account. This is neglected for charged hadrons. All charged particle trajectories are bent in the Earth's magnetic field. The time update is handled for all particles in the same straightforward way. If particles cross an observation level while being tracked to the next interaction point, their space, momentum, and time coordinates are computed for the observation level and transferred to the particle output file.

3.1 Ionization energy loss

The energy loss by ionization of a charged particle which traverses matter of thickness λ is described by the Bethe-Bloch stopping power formula

$$dE_i = \frac{\lambda z^2}{\beta^2} \kappa_1 \left(\ln(\gamma^2 - 1) - \beta^2 + \kappa_2 \right) = \frac{\lambda \gamma^2 z^2}{\gamma^2 - 1} \kappa_1 \left(\ln(\gamma^2 - 1) - \beta^2 + \kappa_2 \right)$$

where $\beta = v/c$ is the velocity of the particle in the laboratory in units of the velocity of light, γ is its Lorentz factor, z is the charge of the ionizing particle in units of e . The two constants $\kappa_1 = 0.153287 \text{ MeV } g^{-1} \text{ cm}^2$ and $\kappa_2 = 9.386417$ are derived from the tables [32] for dry air. This expression is used to compute the ionization energy loss along the particle trajectory. High energy muons with a Lorentz factor $\gamma > 2 \cdot 10^4$ suffer from an additional energy loss by bremsstrahlung (see section 7.1.1) and direct e^+e^- pair formation (see section 7.1.2). The energy loss of muons as function of their energy is given in Figure 3.1. Whenever, after updating the energy, the corresponding Lorentz factor is below the cut-off value, the particle is dropped from the calculation.

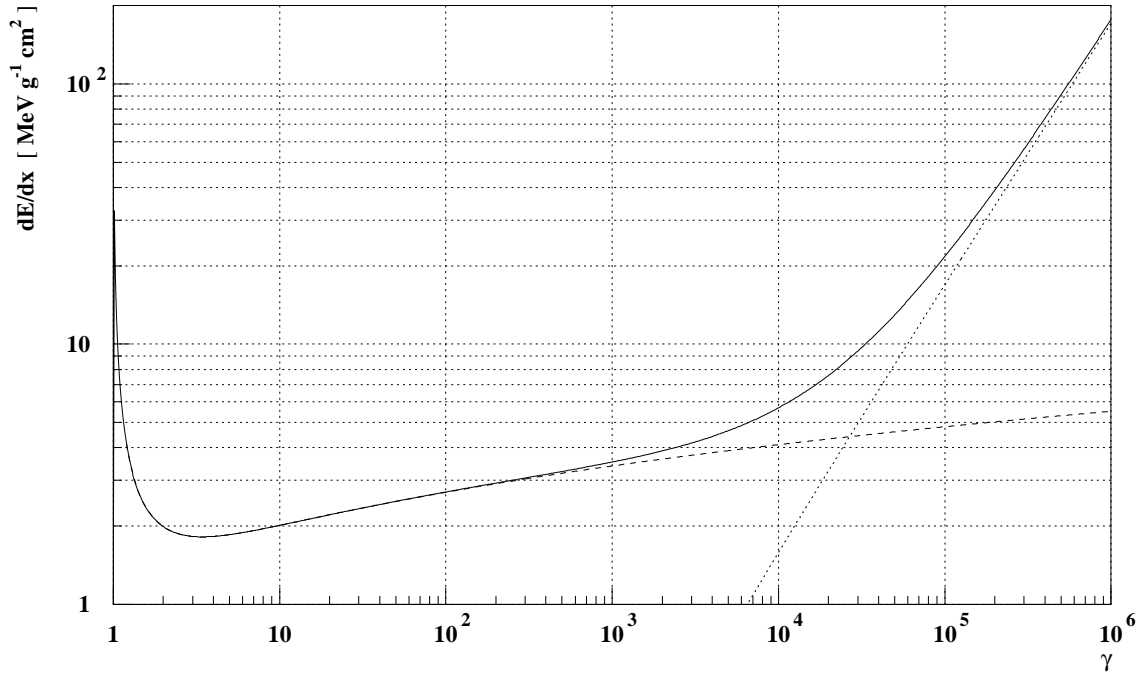


Figure 3.1: Energy loss of muons in air as function of Lorentz factor. The contributions from ionization (dashed line) and direct pair production (dotted line) are indicated.

3.2 Coulomb multiple scattering

Charged particles are scattered predominantly in the electric Coulomb field of the nuclei in the (traversed medium) air. As these nuclei are generally much more massive than the scattered particles, the direction of flight might be altered, but not the energy. In CORSIKA the process of Coulomb multiple scattering is considered only for muons and only once for each tracking step in the middle of the tracking distance. The angular distribution of the multiple scattering is described by Molière's theory [33] or may alternatively (selectable) may be approximated by a Gaussian function. Only about 2% of the events with large scattering angle occur more frequently than predicted by a Gaussian. The procedure to select the scattering angle is taken from the detector simulation code GEANT3 [24]. For heavy particles at high energies multiple scattering is not important. The multiple scattering of electrons is treated very detailed in EGS4 according to Molière's theory.

3.2.1 Molière scattering

The determination of the scattering angle follows Ref. [24]. First, the number Ω_0 of scatterings along the traversed matter of thickness λ is calculated according to

$$\Omega_0 = 6702.33 \frac{\lambda}{\beta^2} \frac{Z_s}{m_{air}} e^{(Z_e - Z_x)/Z_s}$$

where β is the velocity of the muon in units of the speed of light and $m_{air} = 14.54$ is the average atomic weight of air. The quantities Z_s , Z_e , and Z_x depend on the atomic fractions n_i of atoms of type i with charge number Z_i in air:

$$\begin{aligned} Z_s &= \sum_{i=1}^3 n_i Z_i (Z_i + 1) \\ Z_e &= \sum_{i=1}^3 n_i Z_i (Z_i + 1) \ln Z_i^{-2/3} \\ Z_x &= \sum_{i=1}^3 n_i Z_i (Z_i + 1) \ln (1 + 3.34 (Z_i \alpha)^2) \quad . \end{aligned}$$

Here α is the fine structure constant. The index i represents the 3 components of air (see section 2.4).

If the number of scattering events is low, i.e. $\Omega_0 \leq 20$, the total scattering angle is taken as geometrical sum of individual scatterings, which are simulated according to section 3.2.2. Otherwise the polar scattering angle θ is sampled from

$$f(\theta) \theta d\theta = \sqrt{\frac{\sin \theta}{\theta}} f_r(\eta) d\eta \quad .$$

Here the first three terms of Bethe's expansion [34] are used for the function $f_r(\eta)$

$$f_r(\eta) = f_r^{(0)}(\eta) + f_r^{(1)}(\eta) B^{-1} + f_r^{(2)}(\eta) B^{-2} \quad .$$

Tabulated values of the three functions $f_r^{(k)}$ are contained in CORSIKA for the range $0 \leq \eta \leq 13$ of the reduced angle η which is defined by

$$\eta = \frac{\theta}{\chi_c \sqrt{B}} \quad .$$

The quantity B is evaluated from

$$B - \ln B = \ln \Omega_0 \quad ,$$

and the critical angle χ_c is defined by

$$\chi_c = \frac{0.00039612 \sqrt{Z_s}}{\beta^2 E \sqrt{m_{air}}} \sqrt{\lambda}$$

with E the muon energy. The actual value of f_r is derived by a four point continued fraction interpolation between the tabulated values. Scattering angles with $\theta > \pi$ are rejected.

The radial deviation from the straight trajectory is computed and the azimuthal angle is selected at random from a uniform distribution. The particle path then approximated by two straight lines following the incident direction to the midpoint of the tracking step and the new direction thereafter.

3.2.2 Plural Coulomb scattering

If the number of scatters is low, Molière's theory is not applicable and we assume a Poisson distributed number j of scattering events around Ω_0 . Assuming a Rutherford cross section σ for single elastic scattering in the material with charge Z we have

$$f(\theta) \theta d\theta = \frac{d\sigma}{\theta} \frac{1}{d\theta} \frac{1}{\sigma} \theta d\theta \quad \text{with} \quad \frac{d\sigma}{\theta d\theta} = 2\pi \left(\frac{2 Z e^2}{E \beta^2 c} \right)^2 \frac{1}{(\theta^2 + \chi_\alpha^2)}$$

with the screening angle χ_α which is calculated from

$$\chi_\alpha^2 = \frac{0.00039612 \sqrt{Z_s m_{air}}}{1.167 E^2 \beta^2 6702.33 Z_s e^{(Z_e - Z_x)/Z_s}} \quad .$$

For each individual scattering we sample θ_j from

$$f(\theta_j) \theta_j d\theta_j = \chi_\alpha^2 \frac{2\theta_j d\theta_j}{(\theta_j^2 + \chi_\alpha^2)^2} \quad ,$$

which leads, with the random number RD , to

$$\theta_j = \sqrt{\chi_\alpha^2 \left(\frac{1}{RD} - 1 \right)}$$

according to Ref. [24]. To get the total polar scattering angle we take the azimuth angles ϕ_j at random from a uniform distribution and add up the projections of θ_j onto the x and y plane. With this total polar scattering angle the further calculation proceeds as described in the previous section 3.2.1.

3.2.3 Gaussian approximation

In the Gaussian approximation the mean square value of the polar scattering angle θ of a given path is calculated according to the expression of Ref. [35]

$$\langle \theta^2 \rangle = \lambda \theta_s^2 \quad \text{with} \quad \theta_s^2 = \frac{1}{\lambda_s} \left(\frac{E_s}{m\gamma\beta^2} \right)^2 \quad .$$

Here $E_s = 0.021 \text{ GeV}$ is the scattering constant, m , γ , and β represent the mass, Lorentz factor and velocity in the laboratory, respectively. λ is the amount of matter traversed by the particle and $\lambda_s = 37.7 \text{ g/cm}^2$. The value for θ is picked at random according to the Gaussian distribution

$$P(\theta, \lambda) = \frac{1}{\sqrt{\pi\theta_s^2 \lambda}} e^{-\theta^2/(\lambda \theta_s^2)} \quad .$$

The azimuthal angle is selected at random from a uniform distribution. The computation of the arrival coordinates x and y is performed analogously to the Molière case.

3.3 Deflection in the Earth's magnetic field

The Earth's magnetic field is characterized by its strength B_E , its declination angle δ , and its inclination angle ϑ . For the KASCADE location these values are at present

$$B_E = 47.80 \mu T \quad \delta = -9' \quad \text{and} \quad \vartheta = 64^\circ 44'$$

corresponding with the components

$$B_x = 20.40 \mu T \quad \text{and} \quad B_z = -43.23 \mu T \quad ,$$

while $B_y = 0$ by definition (see section 2.3). Because of the small value of δ the deviation of the x-direction from the geographic north may be neglected. Values for other locations may be obtained from the program Geomag, which is available on-line in the world wide web [36].

A particle with charge Z and momentum \vec{p} travelling along the path length ℓ in the magnetic field \vec{B} suffers a deflection which points to the direction normal to the plane spanned by \vec{B} and \vec{p} . The direction is changed by the angle α which, for small deflection angles, is approximately given by

$$\alpha \approx \ell Z \frac{\vec{p} \times \vec{B}}{p^2} \quad .$$

3.4 Time of flight

At the first interaction of the primary in the atmosphere the timing of the shower is started. The time interval dt which elapses as the particle moves along its path is computed by dividing the particular path length ℓ by the average particle velocity β_{ave} . Thus,

$$dt = \frac{\ell}{c\beta_{ave}}$$

where β_{ave} is the arithmetic mean of the laboratory velocities of the particle at beginning and end of the trajectory.

The total time elapsed since the first interaction is the sum of all time intervals accumulated by the successive particles to the particular observation level.

3.5 Longitudinal development

At a selectable step width (in g/cm^2) the longitudinal development of EAS may be followed by sampling the number of gammas, positrons, electrons, negative and positive muons, hadrons, all charged particles, nuclei, and Cherenkov photons traversing each of these sampling altitudes. A function of the type

$$N(T) = N_{max} \left(\frac{T - T_0}{T_{max} - T_0} \right)^{\frac{T_{max} - T}{a + bT + cT^2}}$$

may be fitted to the ‘all charged’ distribution to describe the dependence on the atmospheric depth T . The resulting 6 parameters N_{max} , T_0 , T_{max} , a , b , and c and the χ^2/dof are stored. If EGS4 is not selected, such a fit is tried for the levels which are used to determine the NKG longitudinal distribution (see section 7.2.2).

3.6 Thin sampling

In Monte Carlo programs for EAS simulation the computing times roughly scale with the primary energy, thus becoming excessive for showers initiated by particles with $E_0 > 10^{16}$ eV. A way out of this problem is the ‘thin sampling’ [37] or ‘variance reduction’ [6]. All secondary particles below an adjustable fraction of the primary energy (thinning level $\varepsilon_{th} = E/E_0$) are exposed to this procedure. If the energy sum of all j secondary particles ¹ falls below the thinning energy

$$\varepsilon_{th} E_0 > \sum_j E_j$$

only one of the secondary particles is followed, selected at random according to its energy E_i with the probability

$$p_i = E_i / \sum_j E_j$$

while all other secondaries are discarded. An appropriate weight $w_i = 1/p_i$ is attributed to the surviving particle, thus conserving energy. More correctly the initial weight of the particle is multiplied by w_i .

If only in part the energy of secondary particles falls below the thinning level, the corresponding particles survive with a probability p_i given by

$$p_i = E_i / (\varepsilon_{th} E_0)$$

and, in case of surviving, get the weight factor $w_i = 1/p_i$. The latter procedure is also applied if the energy sum of the corresponding particles exceeds the thinning level, thus enabling more than one particle to survive.

¹Particles not taken into account like neutrinos or falling below the cut-off are excluded from the sum.

ε_{th}	none	10^{-6}	10^{-5}	10^{-4}	10^{-3}
Time (<i>min</i>)	98	51	7.2	1.2	0.16

Table 3.1: Computing times for various thinning levels.

By this selection mechanism only a rather constant number of particles must be followed in the low energy portion of EAS instead of an exponentially growing bulk. This mechanism is implemented in the hadronic part as well as in the EGS4 routines of Ref. [6]. Table 3.6 shows the dependence of the computing time on ε_{th} for $E_0 = 10^{15}$ eV proton showers at vertical incidence employing the QGSJET hadronic interaction model and the EGS4 routines at default CORSIKA parameters.

Chapter 4

Mean free path

The distance a particle travels before it undergoes its next inelastic interaction or decay is determined by the cross section for a hadronic reaction together with the atmospheric density distribution along the flight path, and the probability to decay. Stable particles can only interact, for unstable ones the two processes compete. A decay length and an interaction length are determined independently at random and the shorter one is taken as the actual path length. By this procedure it is also decided whether a particle decays or interacts.

Electrons and photons are treated in the EGS4 routines. A description of the processes they may suffer can be found in [6]. Additional information is given in section 7.2.1.

4.1 Muons

As inelastic hadronic interactions of muons are very rare they are omitted in CORSIKA. Therefore muons may only decay or undergo bremsstrahlung and e^+e^- -pair production interactions. The interaction cross sections σ_{int} for bremsstrahlung and e^+e^- -pair production are calculated in Ref. [38]. We use the parametrizations from the detector simulation code GEANT3 [24]. The mean free path λ_{int} for these interactions is given by

$$\lambda_{int} = m_{air}/\sigma_{int}$$

where $m_{air} = 14.54$ is the average atomic weight of air in g/mol and λ_{int} is given in g/cm^2 . The probability of the muon to traverse an atmospheric layer of thickness λ without corresponding interaction is then

$$P_{int}(\lambda) = \frac{1}{\lambda_{int}} e^{-\lambda/\lambda_{int}} \quad . \quad (4.1)$$

Relativistic muons may propagate through a large fraction of the atmosphere. As we use an atmosphere composed from different layers, a transportation step may only reach at maximum to the next layer boundary or a detection level. Additionally, the

transportation step is limited to $10 \cdot \lambda_s = 377 \text{ g/cm}^2$ to treat the multiple scattering correctly (see section 3.2.3).

If decay determines the path length ℓ , its mean is defined by

$$\ell_D = c\tau_\mu\gamma_\mu\beta_\mu \quad (4.2)$$

where c is the vacuum speed of light, τ_μ is the muon life time at rest, γ_μ is its Lorentz factor and β_μ its velocity in units of c . The probability of a muon to travel the distance ℓ before it decays is then

$$P_D(\ell) = \frac{1}{\ell_D} e^{-\ell/\ell_D} \quad (4.3)$$

and the path length of a muon may be chosen at random from this distribution. It should be noted that in the above formulas ℓ has the dimension of cm . The path lengths are expressed in units of g/cm^2 by taking into account the actual density and its variation along the trajectory. For a given path length ℓ in cm one obtains the path length λ in g/cm^2 as

$$\lambda = f(\ell, h_0, \theta) = \frac{T(h) - T(h_0)}{\cos \theta}$$

with $h = h_0 - \ell \cos \theta$. It depends on the altitude of its origin h_0 and the direction of propagation. The mass overburden $T(h)$ is given by Equation 2.1 or 2.2. The probability distribution for the decay distance λ in g/cm^2 is then

$$P_D(\lambda) = P_D(\ell) \frac{d\ell}{d\lambda} = P(f^{-1}(\lambda)) \frac{df^{-1}(\lambda)}{d\lambda}$$

where f^{-1} represents the inverse function of f . This consideration is only valid, if the kinetic energy of the muons does not change during transport.

In reality in Equation 4.2 γ_μ and β_μ are functions of ℓ itself and one obtains a shorter decay length. In good approximation [39] we determine ℓ in a manner that

$$\int_0^\ell \frac{d\ell}{\beta(\ell)\gamma(\ell)} = -c\tau_\mu \ln(RD) \quad (4.4)$$

where the term at the right side determines at what time in the muon rest frame the decay happens. The Lorentz factor $\gamma(\ell)$ results from

$$\gamma(\ell) = \gamma_0 + \frac{dE}{dx}(\gamma_0) \frac{T(h) - T(h_0)}{m_\mu \cos \theta}$$

with $\frac{dE}{dx}(\gamma_0)$ the ionization loss per radiation length, $T(h_0)$ the mass overburden of the atmosphere and γ_0 the Lorentz factor of the muon at the starting point. $T(h)$ gives the thickness in the altitude $h = h_0 - \ell \cos \theta$, m_μ is the muon mass, and θ the

zenith angle of the muon. Neglecting the change of dE/dx along a transport step and assuming $\beta \approx 1$ the muon range can be calculated analytically in an atmosphere with an exponential density profile¹. With this assumption Equation 4.4 results in

$$-c\tau_\mu \ln(RD) = \int_0^\ell \frac{d\ell}{\beta\gamma} \approx \int_0^\ell \frac{d\ell}{\gamma(\ell)} = \frac{c_i}{d_i \cos \theta} \ln \left(\frac{\gamma_0(d_i - \gamma)}{\gamma(d_i - \gamma_0)} \right) \quad (4.5)$$

where d_i is defined by

$$d_i = \gamma_0 - \frac{dE}{dx}(\gamma_0) \frac{T(h_0) - a_i}{m_\mu \cos \theta} = \gamma_0 + \epsilon_i \quad .$$

a_i and c_i are the atmospheric parameters for layer i defined by Equation 2.1. Solving Equation 4.5 for the Lorentz factor γ delivers

$$\gamma = \frac{\gamma_0 d_i}{\gamma_0 + \epsilon_i \exp(c\tau_\mu \ln(RD) d_i \cos \theta / c_i)} \quad . \quad (4.6)$$

At the bottom boundary h_i of the atmospheric layer i the Lorentz factor is reduced by ionization energy loss (using the Bethe-Bloch stopping power formula Equation 3.1 with the constants κ_1 and κ_2) to

$$\gamma_i = \gamma_0 - \frac{T(h_i) - T(h_0)}{m_\mu \cos \theta} \frac{\gamma_0^2}{\gamma_0^2 - 1} \kappa_1 \left(\ln(\gamma_0^2 - 1) - \beta^2 + \kappa_2 \right) \quad . \quad (4.7)$$

If the Lorentz factor of Equation 4.6 exceeds that of Equation 4.7, the muon decays within the layer i , otherwise for the layer $i - 1$ below that boundary the quantity $c\tau_\mu \ln(RD)$ is replaced by

$$[c\tau_\mu \ln(RD)]_{i-1} = [c\tau_\mu \ln(RD)]_i - \frac{h_0 - h_i + c_i \ln(\gamma_0/\gamma_i)}{d_i \cos \theta} \quad (4.8)$$

and starting with the parameters at the lower boundary of layer i the muon is followed down through the next layer beneath until it decays, undergoes a pair formation or bremsstrahlung event, or reaches the observation level. As the interactions are stochastic processes, they are treated separately in sections 7.1.1 and 7.1.2.

4.2 Nucleons and nuclei

The slowing down of the hadronic projectiles along their path through the atmosphere is taken into account. Because of the reduced energy this leads to a modified cross section and hence to a modified free path. In contrast to the muon decay length this effect is omitted for hadronic interactions. At energies above $\approx 100 \text{ GeV}$

¹For other density profiles see Appendix B.

the cross sections decrease with decreasing energy and the ionization energy losses would result in a slightly increased range of the hadrons. As the cross sections vary very moderately with energy and the ionization energy losses are small compared to the kinetic energy of the hadrons, it is justified to neglect the ionization energy losses. The free paths of nucleons or nuclei as stable particles are determined by their inelastic nucleon-air or nucleus-air cross section only.

4.2.1 Nucleon-air cross section at high energies

Depending on the employed hadronic interaction model different parametrizations of the cross sections are used. In all cases the cross section is taken as the weighted sum over the cross sections σ_{n-N_i} of the components of air

$$\sigma_{n-air} = \sum_{i=1}^3 n_i \sigma_{n-N_i} \quad (4.9)$$

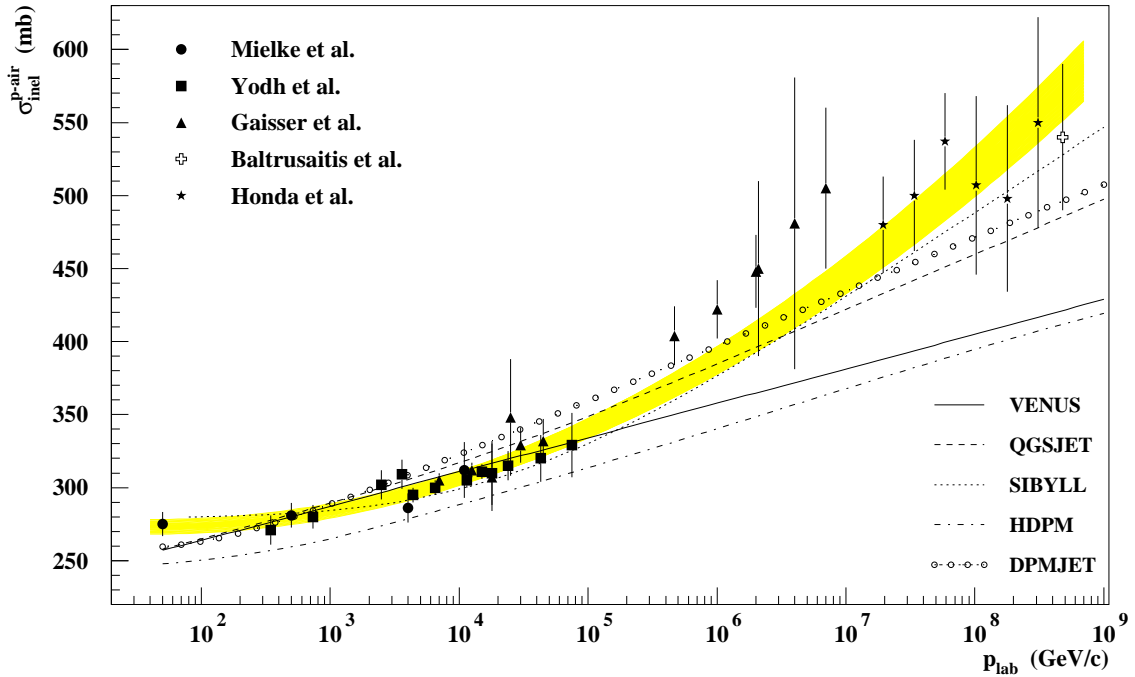


Figure 4.1: Inelastic proton-air cross sections for the models used in CORSIKA as a function of projectile momentum. The experimental data are taken from Refs. [40, 41, 42, 43, 44]. The shaded band represents the result of a fit of the form $\sigma_{inel}^{p-air} = a \log(p) + b \log^2(p) + c$ to the data with $p < 10^5 \text{ GeV}/c$. For HDPM see footnote in Appendix C.

with n_i the atomic fraction of component i . The available nucleon-air cross sections are shown in Fig. 4.1 together with experimental data. They include the diffractive contribution as given by each of the different models. If not specified, the default cross sections (HDPM) as described in Appendix C are used. The interaction mean free path λ_{int} is obtained from the nucleon-air cross sections by

$$\lambda_{int} = m_{air}/\sigma_{n-air} \quad (4.10)$$

where $m_{air} = 14.54$ is the average atomic weight of air in g/mol and λ_{int} is given here in g/cm^2 . The probability of the projectile to traverse an atmospheric layer of the thickness λ without interaction is then

$$P_{int}(\lambda) = \frac{1}{\lambda_{int}} e^{-\lambda/\lambda_{int}} \quad . \quad (4.11)$$

From this distribution, the path lengths of nucleons are chosen at random. The interacting target nucleus is randomly selected according to the contribution of each air component to the sum of Equation 4.9.

4.2.2 Nucleon-air cross section at low energies

Using the GHEISHA package below $E_{lab} \leq 80 GeV$, the interaction cross sections are interpolated from tables supplied with GHEISHA [12]. They comprise elastic and inelastic interactions and include slow neutron capture processes in a rather realistic manner as derived from experimental data. They are plotted in Fig. 4.2.

Employing the ISOBAR model, the inelastic cross sections as given in Appendix C are used. The measured inelastic nucleon-nucleon cross section drops rapidly with decreasing energy. Therefore below $p_{lab} = 10 GeV/c$ the ISOBAR model allows only elastic reactions with a constant cross section. For antinucleons an annihilation with nucleons can occur in addition, leading to a contribution to the inelastic cross section which rises with decreasing energy. These cross sections are also shown in Fig. 4.2.

4.2.3 Nucleus-nucleus cross section

In EAS nucleons or complex nuclei are reacting with air nuclei. In the energy range of interest no experimental data exist on the relevant quantities, such as inelastic cross section and number of target and projectile nucleons participating in the reaction. So they have to be calculated from the nucleon-nucleon cross section following Glauber theory [45, 46]. The input nucleon distributions of nuclei are derived from measured charge distributions [47] unfolding the finite size of the proton with a mean square charge radius of $\langle r_p^2 \rangle^{1/2} = 0.862 fm$. For nuclei with mass number below 20 the charge distributions are assumed to be Gaussian and the radius of the nucleon distribution is

$$\langle r_m \rangle^2 = \langle r_{ch} \rangle^2 - \langle r_p \rangle^2 \quad .$$

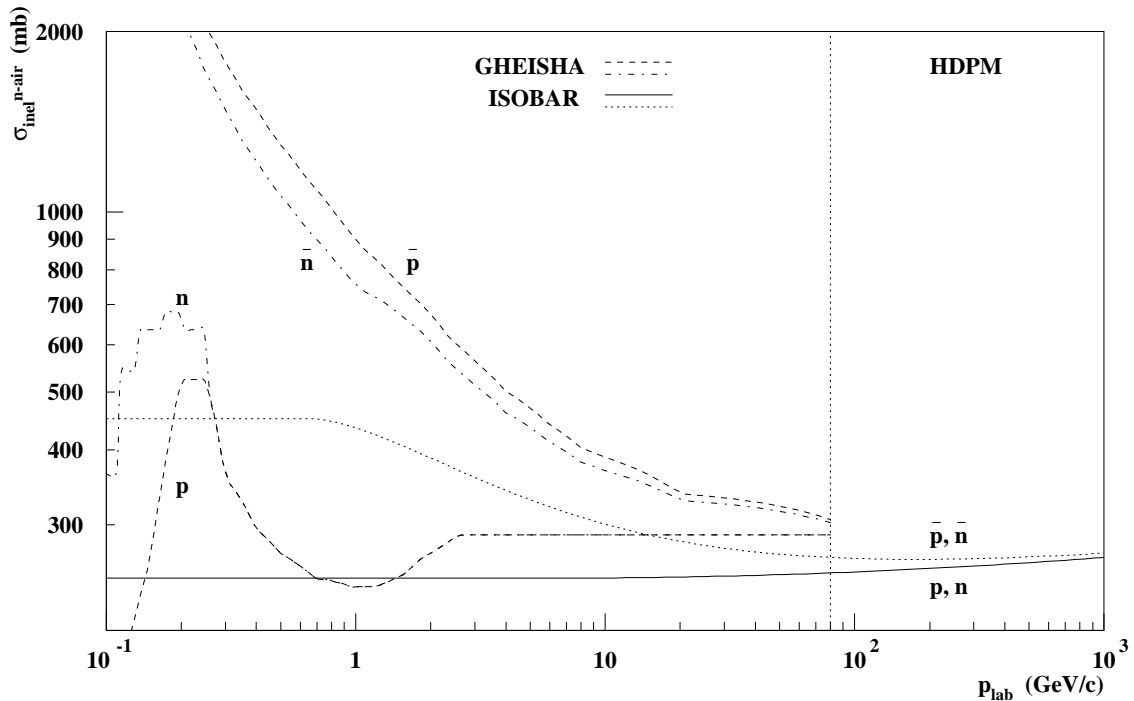


Figure 4.2: Inelastic nucleon-air cross sections at lower energies. The cross sections of the GHEISHA model are drawn for protons, anti-protons (dashed lines), neutrons, and anti-neutrons (dashed-dotted lines) together with the cross sections of the ISOBAR and HDPM model for nucleons (solid line) and anti-nucleons (dotted line). The dotted vertical line marks the boundary between high energy and low energy hadronic interaction models.

For nuclei with $A > 20$ the charge distributions are approximated by the Fermi function. Unfolding was done by folding a correspondingly parametrized nucleon distribution with the proton charge distribution to obtain the measured radius and diffuseness of the charge distribution of the nucleus. From the Glauber method the inelastic cross sections for all projectile nuclei in the stability valley with $A = 1 \dots 56$ colliding with the target nuclei ^{14}N , ^{16}O , and ^{40}Ar were calculated for three different values of the nucleon-nucleon cross section (30, 45, and 60 mb ; they correspond to nucleon-nucleon collisions at laboratory energies of 120 GeV , 66.5 TeV , and 5.87 PeV , respectively, for the HDPM generator). Values for mass numbers for which no experimental charge distributions were available have been interpolated. The results are tabulated in CORSIKA and a quadratic interpolation is performed between the table values with respect to σ_{n-n} to obtain intermediate values of the cross section σ_{N-N_i} of a nucleus with component i of air. Then σ_{N-air} is obtained

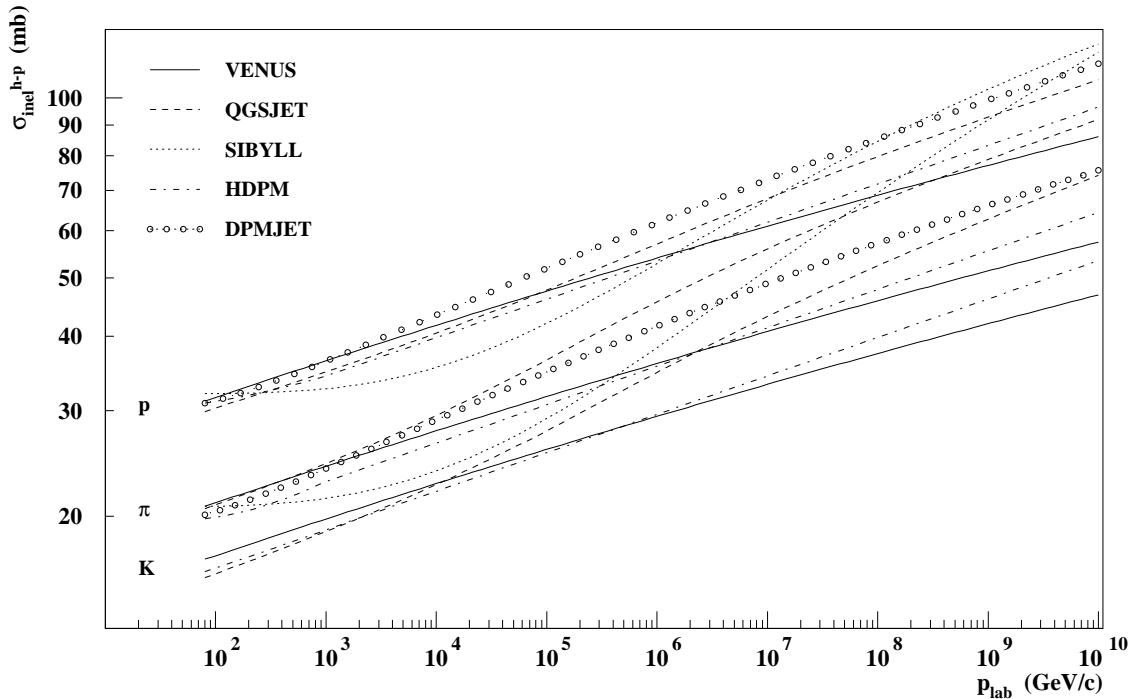


Figure 4.3: Inelastic cross sections of protons, pions, and kaons with protons for the models used in CORSIKA as function of projectile momentum. For HDPM see footnote in Appendix C.

from the weighted sum over the three components of air

$$\sigma_{N-air} = \sum_{i=1}^3 n_i \sigma_{N-N_i} \quad . \quad (4.12)$$

The SIBYLL model provides its own nucleus-nucleus cross section table including an interpolation routine, while for the other models we use the model-specific nucleon-nucleon cross section and apply our Glauber formalism to get the desired nucleus-nucleus cross section. The used proton-proton cross sections are shown in Fig. 4.3. The resulting nucleus-air cross sections are shown in Figure 4.4. For DPMJET and VENUS it is possible to calculate model specific nucleus-nucleus cross sections in a time consuming manner. They differ from the cross sections shown in Fig. 4.4 by $< 8 \%$.

The interaction mean free path λ_{int} is obtained by

$$\lambda_{int} = m_{air} / \sigma_{N-air}$$

where $m_{air} = 14.54$ is the average atomic weight of air in g/mol and λ_{int} is given here in g/cm^2 . This is done for high energy interaction models. In GHEISHA and

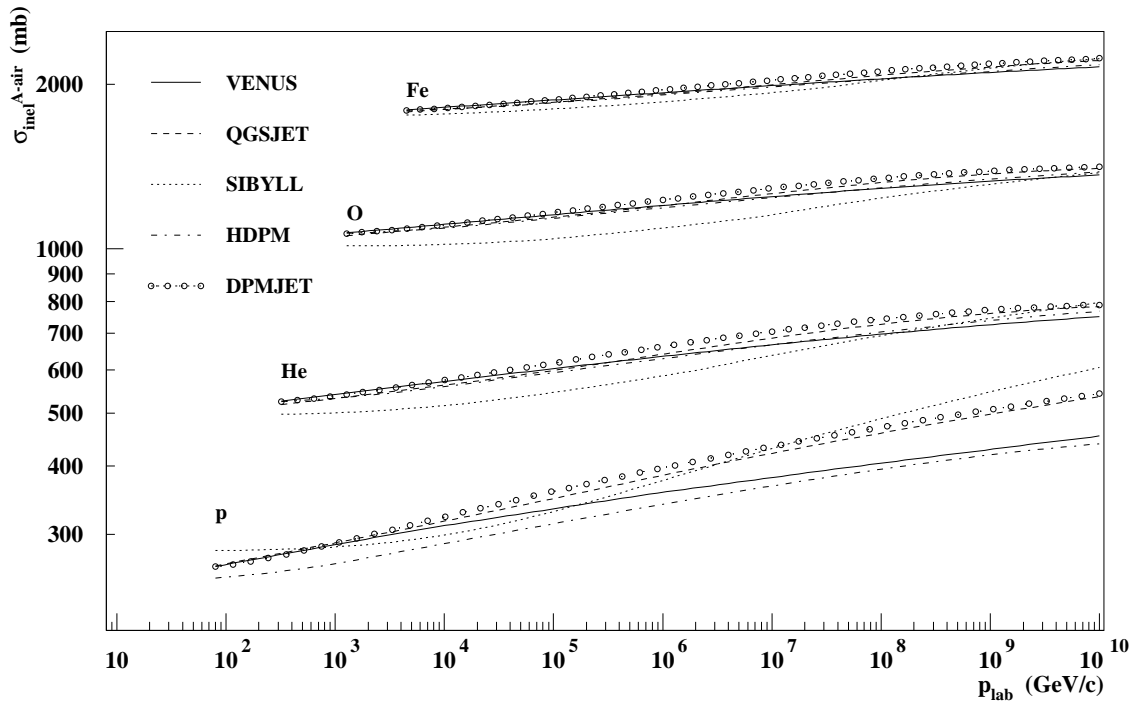


Figure 4.4: Inelastic nucleus-air cross sections of various projectile nuclei for the models used in CORSIKA as function of projectile momentum. For HDPM see footnote in Appendix C.

ISOBAR only nucleon-nucleon interactions are treated. The path lengths of projectile nuclei are sampled from an appropriate distribution. The interacting target nucleus is randomly selected according to the contribution of each air component to the sum of Equation 4.12.

In the treatment of hadron-nucleus and nucleus-nucleus collisions by the various models, the number of interacting target and projectile nucleons is determined by the selected model. SIBYLL and HDPM treat nucleus-nucleus collision as a superposition of nucleon-nucleus collisions.

4.3 Pions and kaons

Charged pions and all four kinds of kaons are particles where decay and nuclear interaction compete. Their decay lengths are determined in the same way as for muons just replacing the free muon life time τ_μ by the pion and kaon life times τ_π and τ_K , respectively. For pions and charged kaons the ionization energy loss is also taken into account in the same manner as for muons.

The interaction lengths are treated in analogy to those of nucleons. They are

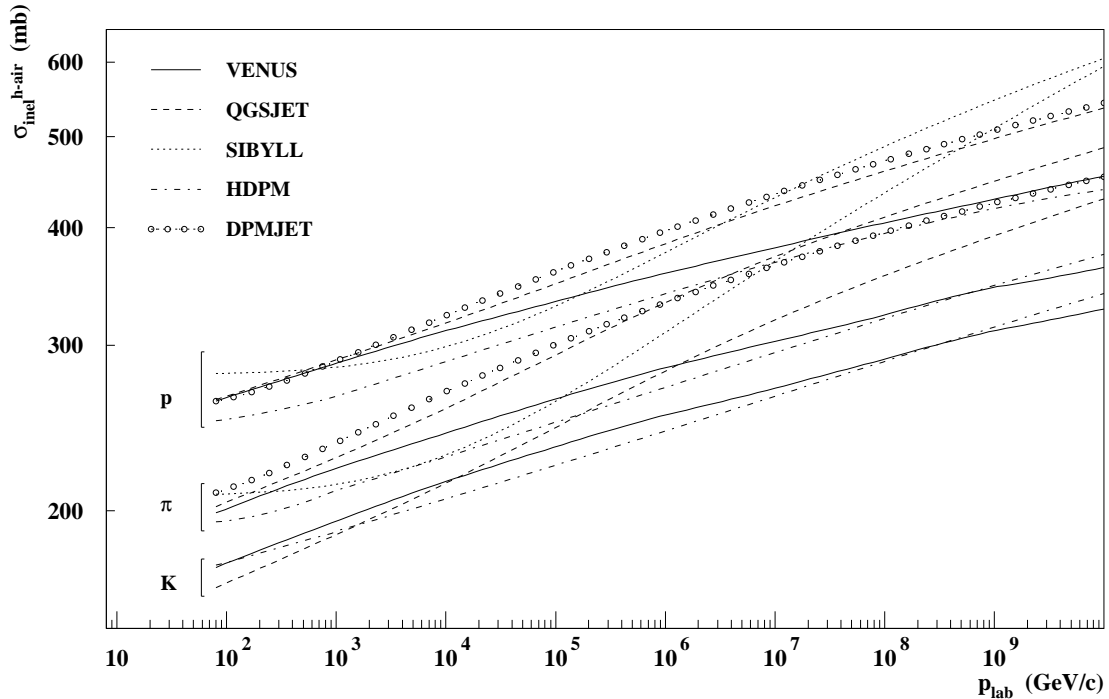


Figure 4.5: Inelastic hadron-air cross sections at higher energies of various interaction models as used in CORSIKA. In SIBYLL and DPMJET the pion cross sections are also used for kaons. For HJPM see footnote in Appendix C.

determined according to Equations 4.10 and 4.11 using the model specific meson-air cross sections as shown in Fig. 4.5. Also the selection of the interacting target nucleus follows section 4.2.1.

Employing the GHEISHA package below $E_{lab} \leq 80 \text{ GeV}$ the interaction cross sections are interpolated from tables supplied with GHEISHA. The resulting pion-air and kaon-air cross sections are shown in Figure 4.6. The actual free path of the meson is taken as the minimum of a random decay length and a random interaction length. By this selection also the decision between decay and interaction is made.

Due to their short life time of neutral pions of $\tau = 8.3 \cdot 10^{-17} \text{ sec}$ their probability for interaction is omitted for $E_{lab} < 10^{14} \text{ eV}$ and they decay at their origin. Above they are tracked by analogy with the charged pions. Above $E_{lab} > 10^{18} \text{ eV}$ their decay length becomes comparable to their interaction length in the lower atmosphere.

4.4 Other hadrons and resonances

The η meson is treated in the same manner as neutral π mesons. Because of their short life time of order of 10^{-23} sec the ρ , K^* , and Δ resonance states decay imme-

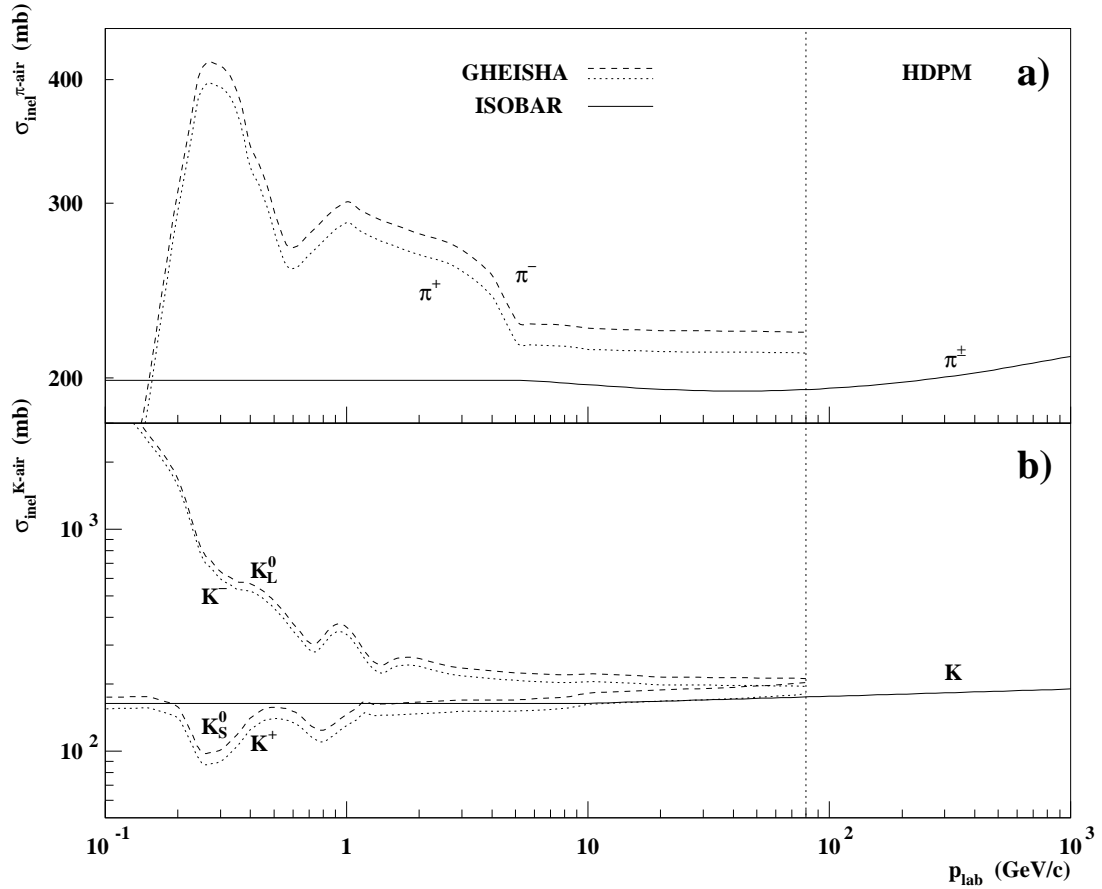


Figure 4.6: Inelastic meson-air cross sections at lower energies for a) pions and b) kaons. The solid lines give the cross section as calculated for the ISOBAR and HDPM model, the dashed and dotted lines lines with signatures give the cross sections as used in the GHEISHA option. The dotted vertical line marks the boundary between high energy and low energy hadronic interaction models.

diately after their production without being tracked.

Baryons with strangeness ± 1 , ± 2 , and ± 3 are produced by most models explicitly, while HDPM knows only hadrons with one strange quark or anti-quark. In spite of their short life time of $\approx 10^{-10}$ sec their mean free path is too long to be neglected. Their decay length is determined analogously to that of π^\pm and kaons, taking into account the ionization energy loss for the charged strange baryons. Their interaction cross sections are adopted to be the same as for nucleons. In the low energy range only the GHEISHA routines are able to treat strange baryons, the corresponding

cross sections are interpolated from the GHEISHA cross section tables.

4.5 Neutrinos

As all kinds of neutrinos have extremely small interaction cross sections, they are assumed to traverse the atmosphere without interaction.

Chapter 5

Hadronic interactions

Hadronic interactions are simulated within CORSIKA by several models depending on energy. If the energy is high enough, the interaction is treated alternatively with one of the models VENUS [7], QGSJET [8], DPMJET [9], SIBYLL [10], or HDPM. The former are well documented and the interested reader is referred to the literature. The last one is described in detail in Appendix D. The high energy models reach their limit, if the cm energy available for generation of secondary particles drops below a certain value. This value is presently set at 12 *GeV* corresponding to a laboratory energy of 80 *GeV* for the transition to GHEISHA. If GHEISHA is replaced by the ISOBAR model the transition energy is lowered to $E_{cm} = 10$ *GeV* resp. $E_{lab} = 50$ *GeV*. In an EAS, however, the bulk of particles interacts at cm energies far below these values.

Below these transition energies the user may select between the GHEISHA routines [12] or the ISOBAR model. The GHEISHA routines as implemented in CORSIKA are taken from the detector simulation code GEANT3 [24]. This detector simulation code is used by many high energy experimental groups, and therefore much experience on the validity of the GHEISHA routines exists. The simple ISOBAR model enables fast calculations and is used for the hadronic interactions as explained in section 5.2.2. It should be noted that the selection of DPMJET, QGSJET, SIBYLL, or VENUS needs (and automatically forces) the GHEISHA option, as the baryons with strangeness ± 2 and ± 3 generated by those models cannot be treated by the ISOBAR model.

5.1 Strong interactions at high energies

Table 5.1 gives an overview on essential features of the available high energy hadronic interaction models. A comparison of the interaction models is given in Refs. [48, 49, 50] and the effects on observables of EAS are discussed there in detail.

	VENUS	QGSJET	DPMJET	SIBYLL	HDPM
Gribov-Regge	+	+	+		+
Minijets		+	+	+	+
Sec. Interactions	+				
N-N Interaction	+	+	+		
Superposition				+	+
Max. Energy (GeV)	2×10^7	$> 10^{11}$	$> 10^{11}$	$> 10^{11}$	10^8

Table 5.1: Basic features of the interaction models used.

5.1.1 VENUS

The VENUS code [7] (**V**ery **E**nergetic **N**uclear **S**cattering) is mainly designed to treat nucleon-nucleon, nucleon-nucleus, and nucleus-nucleus scattering at ultrarelativistic energies. It is based essentially on the Gribov-Regge theory, which considers single or multiple Pomeron exchange as the basic process in high energy hadron-hadron scattering. A Pomeron is represented by a cylinder of gluons and quark loops according to the topological expansion of quantum chromodynamics. Particle production in inelastic collisions amounts to cutting Pomerons, i.e. cutting cylinders, which in VENUS is realized by forming colour strings which subsequently fragment into colour neutral hadrons. At high densities, for collisions of heavy nuclei, when independent binary interactions become unlikely, massive quark-matter droplets may be formed. Final state interactions are taken into account. Diffractive and non-diffractive collisions as well as mesonic projectiles are described with the same formalism. This leads to a consistent and theoretically well founded treatment of all types of hadronic reactions involved in an air shower cascade. As jets which become important at extremely high energies are not contained within this model, we recommend an upper limit of $E_{lab} < 2 \cdot 10^{16}$ eV for the projectile.

All mesons and baryons known to the CORSIKA program (see section 2.2) may be used as projectiles in VENUS. Moreover also nuclei are admitted. Neutral K_{SL}^0 mesons are regarded as K^0 or \bar{K}^0 particles with equal probabilities. Photons undergoing hadronic reactions are treated as π^0 or η with equal chance (see section 7.2.1). The parameter w_{proj} which enters into the determination of the probability of diffractive interaction of the projectile, is set to 0.32 for baryons, to 0.24 for strange mesons, and to 0.20 for pions. The latter two values have been adjusted to reproduce experimental Feynman x distributions of secondaries at projectile energies of $E_{lab} = 250$ GeV [51]. The spectator nucleons surviving from primary nucleus projectiles may be treated by various fragmentation options as described in section 5.3.

Structure function integrals

The presently implemented version¹ of VENUS uses the Duke-Owens parametrization [52] of the parton distribution functions for sea and valence quarks with flavour $i \in \{u, d, s, \bar{u}, \bar{d}, \bar{s}\}$ as

$$f_i^{sea/val}(z) = \frac{A_i z^{a_i} (1-z)^{b_i} (1+\alpha_i z)}{\sqrt{z^2 + 4\mu^2/s}}$$

where A_i , a_i , b_i , and α_i are parameters adjusted to experimental values; μ is a cutoff parameter of the order of 1 GeV, and s is the squared energy in the cm system. The original VENUS code uses a rather time consuming numerical integration to evaluate the structure function integrals $I(s, x)$

$$I(s, x) = \int_0^x f_i(z) dz$$

at the beginning of a run to perform many collisions at a constant energy. In EAS the energy varies from collision to collision, and hence we need these integrals several thousand times for a complete shower. To accelerate the calculation we make use of special properties of the integrals. For the sea quarks the exponents b_i attain approximately integer values and the integrals are (to good approximations) evaluated analytically. In the valence quark case we keep the integrals as tables for a set of x values in the range $0 \leq x \leq 1$, calculated for $s \rightarrow \infty$ with high precision. For each individual case of $s = E_{cm}^2$ we add a correction term ΔI , which depends on the collision energy like

$$\Delta I = -\exp(c_1 + c_2 \ln p_{lab})$$

with fitted constants c_1 and c_2 and p_{lab} the projectile laboratory momentum. This term is analytically evaluable, and the integrals are sufficiently well approximated for $x \geq 5x_{cut} = 20\mu^2/s$. For the few cases with x values below this limit the valence quark structure function integrals must be evaluated numerically. Mainly by these means, the computing time for a single collision at $E_{lab} = 10^{15}$ eV is reduced to $\leq 4\%$ for proton projectiles and to $\leq 25\%$ for iron nuclei projectiles.

5.1.2 QGSJET

QGSJET (Quark Gluon String model with JETs) is an extension of the QGS model [53, 54], which describes hadronic interactions on the basis of exchanging supercritical Pomerons. Pomerons are cut according the Abramovskiĭ-Gribov-Kancheli rule and form two strings each. These strings are fragmented by a procedure similar to the Lund algorithm [55, 56], but with deviating treatment of the momenta at the string

¹VENUS version 4.12, released April 9, 1993

ends. Additionally QGSJET [8] includes minijets to describe the hard interactions which are important at the highest energies.

In the case of nucleus-nucleus collisions the participating nucleons are determined geometrically by Glauber calculations, assuming a Gaussian distribution of the nuclear density for the light nuclei with $A \leq 10$ and a Woods-Saxon distribution for the heavier nuclei. The collision is treated by application of the percolation-evaporation fragmentation mechanism [57] of the spectator parts of the involved nuclei. Thus in peripheral collisions spallation like reactions happen, while in central collisions a more or less complete fragmentation into many small fragments takes place. To these fragments the various fragmentation options may be applied as described in section 5.3.

5.1.3 DPMJET

DPMJET (**D**ual **P**arton **M**odel with **J**ETs Version II.4) is based on the two component Dual Parton Model [9, 58, 59] and contains multiple soft chains as well as multiple minijets. As VENUS and QGSJET, it relies on the Gribov-Regge theory and the interaction is described by multi-Pomeron exchange. Soft processes are described by a supercritical Pomeron, while for hard processes additionally hard Pomerons are introduced. High mass diffractive events are described by triple Pomerons and Pomeron loop graphs, while low mass diffractive events are modelled outside the Gribov-Regge formalism. Cutting a Pomeron gives two strings, which are fragmented by the JETSET routines [60] according to the Lund algorithm [55, 56].

If nuclei are involved in a collision the number of participating nucleons as well as the number of nucleon interactions is obtained by Glauber theory using the algorithm of Ref. [61]. The refined treatment of the residual nuclei by the formation zone intranuclear cascade model [62] takes into account the nuclear excitation energy, models nuclear evaporation, high energy fission and break-up of light nuclei, and emission of deexcitation photons for projectile and target nuclei. This might be of some importance for projectiles in light-ion induced EAS [63]. For comparative studies also the various fragmentation options are available (see section 5.3). The effects of the various fragmentation options on the measurable quantities of EAS are discussed in Ref. [64].

Short living secondaries not known within CORSIKA are to decay within DPMJET. DPMJET produces also charmed hadrons which cannot be treated by CORSIKA. Therefore within these charmed hadrons the charm quark is replaced by a strange quark and the modified strange hadrons are tracked and undergo interactions or decays within CORSIKA.

5.1.4 SIBYLL

SIBYLL (Version 1.6) [10, 11] is a minijet model essentially designed for usage in EAS Monte Carlo programs. For hadronic soft collisions both projectile and target

particles fragment into a quark-diquark resp. quark-antiquark system, that forms a triplet and anti-triplet of colour. The components of opposite colour of the two hadrons are then combined to form two colour strings that are fragmented according to a slightly modified version of the Lund algorithm [55, 56]. Additional strings originating from hard collisions with minijet production with high p_T are considered. The rise of the inelastic cross section with energy is fully attributed to an increasing number of minijets, while the contribution of the soft component is assumed to be energy independent. Diffractive events are modelled independently of soft or hard collisions.

In hadron-nucleus collisions the number ν of interacting target nucleons determines the number of soft strings: Each participating target nucleon is split into two components, while the projectile is split into 2ν components: two valence components that carry the quantum numbers of the incident projectile, and $(\nu - 1)$ quark-antiquark component pairs. Again these partons are joined in pairs of strings with opposite colour coupling projectile and target components, and these strings are fragmented.

Nucleus-nucleus interactions are treated in a semi-superposition model, where the number of interacting projectile nucleons is determined by Glauber theory, while the projectile spectator nucleons fragment into light to medium heavy nuclei according to a thermal model [11]. Moreover the various fragmentation options as described in section 5.3 are available.

Short lived secondary particles produced by SIBYLL decay immediately into particles which are known within CORSIKA (see section 2.2), but only nucleons and antinucleons, charged pions, and all four species of kaons can be treated as projectiles by SIBYLL. Other particles like strange baryons are tracked but only decay and no interaction is admitted. In photonuclear interactions the incident gamma ray is substituted by a charged π .

5.1.5 HDPM

As an alternative model of the interactions between hadrons and nuclei at high energies, a phenomenological generator called HDPM may be used. For historical reasons it is the default. It is developed by Capdevielle [4] and inspired by the Dual Parton Model [5]. The HDPM routines are usable up to $E_{lab} \approx 10^{17}$ eV. A detailed description of the physical ideas and the parameters adjusted to results of $p\bar{p}$ -collider experiments up to $E_{lab} \approx 2 \cdot 10^{15}$ eV is given in Appendix D.

5.2 Strong interactions at low energies

5.2.1 GHEISHA

The GHEISHA package is recommended for the treatment of low energy hadronic interactions. We coupled it to CORSIKA in the same way as it is implemented into

the detector simulation code GEANT3 [24]. The GHEISHA routines [12] are designed for laboratory energies up to some hundred GeV . We use them only at laboratory energies below $80 GeV$ to treat the interactions of hadronic projectiles with the nuclei of the atmosphere. All hadronic projectiles including baryons with strangeness ± 1 , ± 2 , and ± 3 can be handled, however nuclear fragments emerging from evaporation processes like d , t , and α particles cannot be treated by GHEISHA. The cross sections for elastic and inelastic interactions are interpolated and extrapolated from tabulated values derived from experimental data and stored within the GHEISHA package. Neutron capture is taken into account as a third process for neutrons with $E_{lab} \leq 0.033 GeV$. As the atmosphere does not contain fissile materials, we have eliminated the routines treating nuclear fission. From the cross sections the type of interaction is chosen at random, and the multiplicity and kinematic parameters of the secondary particles are sampled with the appropriate GHEISHA reaction routine.

The GHEISHA routines treat low energy neutrons in a very consistent way. This must be compared with the ISOBAR model, in which the low energy neutrons are scattered around without energy loss in a rather unrealistic manner, thus resulting in numerous low energy neutrons. Therefore we recommend the use of the GHEISHA option despite the longer calculation times.

It should be noted, that in GHEISHA only the elements H, Al, Cu, and Pb are tabulated as target materials and that the interesting cross section data for the target elements N, O, and Ar which compose the atmosphere must be obtained by interpolation, with a loss of accuracy. In standard high energy physics experiments air is not employed as target or detector material, therefore a check on the validity of this interpolation is impeded.

5.2.2 ISOBAR

The routines of the ISOBAR model of Griener [3] work at cm energies between $0.3 GeV$ and $10 GeV$. In this model the hadron-nucleus collisions are approximated by hadron-nucleon reactions. The non-interacting nucleons of the target are neglected. The hadron-nucleon reactions are assumed to take place via several intermediate states which are decaying immediately into up to 5 secondaries. The intermediate state can be a single particle, a heavy non-strange or strange meson, or a light or a heavy ISOBAR. Intermediate states produced simultaneously share the available cm energy according to their masses and move only forward or backward with respect to the laboratory direction. These intermediate states cannot be identified with single well established particles or resonances, but are to represent the manifold of short lived states observed in this energy region which decay mostly into few secondaries. Details on the mass parameters of these isobars, on their decay into secondary particles, on the selection of transverse momenta, and on the annihilation of antinucleons are given in Ref. [21]

5.3 Nuclear fragmentation

For the non-interacting nucleons of a projectile nucleus, the so called spectators, various options exist [65]. First, they can be regarded as free nucleons with their initial velocity. They are stored on the internal particle stack and are processed further at a later time. This option assumes the ‘total fragmentation’ of the projectile nucleus in the first interaction. A second option, ‘no fragmentation’, keeps all spectators together as one nucleus propagating further through the atmosphere and reacting later on. These two options, being the limiting cases of what really happens in nature, allow to estimate the influence of the nuclear fragmentation on the results of the air shower simulations. Our calculations show that the differences between the two cases are small and details of fragmentation are smeared out by fluctuations.

Two further options keep also the spectator nucleons together, but calculate the excitation energy of this remaining nucleus from the number of wounded nucleons in a way as described in Ref. [66]. Each wounded nucleon is assumed to be removed out of the Woods-Saxon potential of the original projectile nucleus, which leads to hole states in the nucleonic energy level system. The depth of the nuclear potential well amounts typically to 40 *MeV*. As hole states may occur in any arbitrary nuclear level, each wounded nucleon contributes with an energy between 0 and 40 *MeV* to the total excitation with equal probability. From this total excitation energy the number of evaporating nucleons or α particles is calculated assuming a mean energy loss per evaporated nucleon of 20 *MeV* [67]. The validity of this treatment is testified [68] in a comparison with data from the CERN EMU07 experiment [69].

The emitted nucleons carry a transverse momentum, which differs in the two available evaporation options following the parametrizations of Refs. [70, 71]. But the global effect of the latter two options - a widening of the lateral distribution of the whole shower compared with the total fragmentation or no-fragmentation options - is usually small as compared to statistical fluctuations [64].

Chapter 6

Particle decays

Most of the particles produced in a high energy interaction are unstable and may decay into other stable or unstable particles. Neutral pions and η mesons as well as all resonance states have such a short life time that interaction is negligible before they decay. Muons are prevented from penetrating the complete atmosphere by decay only. Neutrons are treated as stable particles due to their long life time. For all the other unstable particles there is a competition between interaction and decay processes and the decision is taken when calculating the actual free path as described in the beginning of chapter 4. If several decay modes exist, all known modes with a branching ratio down to 1% are taken into account. In this section we describe the treatment of particle decays in CORSIKA.

6.1 π^0 decays

Neutral pions decay predominantly (98.8 %) into 2 photons $\pi^0 \longrightarrow \gamma + \gamma$. This decay is isotropic in the cm system of the π^0 . There, the photon energy is $E_{\gamma cm} = m_{\pi^0}/2$ and the angle with respect to the direction of motion in the laboratory system is θ_{cm} . In the laboratory system which moves with β_{π^0} with respect to the cm system the energies and angles of the photons can be found by Lorentz transformation

$$\begin{aligned} E_{\gamma lab}^i &= \frac{1}{2} \gamma_{\pi^0} m_{\pi^0} (1 \pm \beta_{\pi^0} \cos \theta_{cm}) \\ \cos \theta_{lab}^i &= \frac{\beta_{\pi^0} \pm \cos \theta_{cm}}{1 \pm \beta_{\pi^0} \cos \theta_{cm}} \quad i = 1, 2 \quad . \end{aligned}$$

The values of $\cos \theta_{cm}$ and the angle ϕ around the incident direction are selected at random to get a uniform distribution over the whole solid angle.

The Dalitz decay $\pi^0 \longrightarrow e^+ + e^- + \gamma$ happens in 1.2 % of the cases only. It is a bit more complicated than the decay into two photons, because the particle energies in the cm system are not fixed, but vary in the kinematically allowed range. However, momentum and energy conservation restrict the three secondary particles to lie in one plane and to share the cm energy. The energies are calculated to fall inside a Dalitz

plot which gives a probability density function for a decay depending on the variables p_{12} , p_{13} where $p_{ik} = p_i + p_k = -p_l$ are the sums of the momenta of two particles each. This probability density function directly depends on the matrix element $|M|^2$ of the decay. As we do not know this matrix element for the π^0 decay, we assume a constant value. The energies of the secondary particles are taken at random from this distribution. The cm values of $\cos\theta$ and angle ϕ of the first secondary particle are chosen at random uniformly in the full solid angle. The angle ψ of the reaction plane around the first particle direction is also chosen at random. As final step, the particle kinematical parameters are transformed to the laboratory system.

6.2 π^\pm decay

The decay $\pi^\pm \longrightarrow \mu^\pm + \nu_\mu$ is a two-body decay, isotropic in the cm system of the pion. Therefore, $\cos\theta_{cm}$ and ϕ_{cm} of the muon are taken from a uniform distribution and the energy is shared between muon and neutrino in a way that their cm momenta add up to zero. This leads to

$$E_{\mu\ cm} = \frac{m_\pi^2 + m_\mu^2}{2m_\pi} = m_\mu \gamma_{\mu\ cm} = 1.039m_\mu$$

and after Lorentz transformation into the laboratory system

$$\begin{aligned} \gamma_{\mu\ lab} &= \gamma_\pi(\gamma_{\mu\ cm} + \beta_\pi \cos\theta_{\mu\ cm} \sqrt{\gamma_{\mu\ cm}^2 - 1}) \\ \cos\theta_{\mu\ lab} &= \frac{\gamma_\pi \gamma_{\mu\ lab} - \gamma_{\mu\ cm}}{\gamma_\pi \beta_\pi \sqrt{\gamma_{\mu\ lab}^2 - 1}} \end{aligned} .$$

The muon carries a longitudinal polarization

$$\xi = \frac{1}{\beta_\mu} \left(\frac{E_{\pi\ lab}}{E_{\mu\ lab}} \frac{2r}{1-r} - \frac{1+r}{1-r} \right)$$

with $r = (m_\mu/m_\pi)^2$ as given in [72]. We calculate the muon spin direction relative to the laboratory frame and assume that this direction is maintained until the muon decays. The calculation of the neutrino kinematical parameters is optional and gives

$$\begin{aligned} E_{\nu\ lab} &= m_\pi \gamma_\pi - m_\mu \gamma_\mu \\ \cos\theta_{\nu\ lab} &= \frac{\beta_\pi - \cos\theta_{\mu\ cm}}{1 - \beta_\pi \cos\theta_{\mu\ cm}} \end{aligned} .$$

6.3 Muon decay

At the end of its track, a muon can only decay via $\mu^\pm \longrightarrow e^\pm + \nu_e + \nu_\mu$. The electron energy distribution in the cm system is [73]

$$\frac{dN_e}{dE_{e\ cm}} \propto 3 \frac{m_\mu^2 + m_e^2}{2m_\mu} E_{e\ cm}^2 - 2E_{e\ cm}^3$$

from which the electron cm energy $E_{e\text{ cm}}$ is taken at random. The direction correlation of this three-body decay is governed by the longitudinal polarization of the muon. The electron emission direction relative to the muon spin is determined with the uniformly distributed angle $\cos \delta$ and with $\zeta = \mp 1$ for μ^\pm to be

$$\cos \theta_{e\text{ cm}} = \zeta \frac{\sqrt{1 + A(2 \cos \delta + A)} - 1}{A} \quad \text{with} \quad A = \frac{1 - 2x}{2x - 3}$$

where x is the ratio of the electron energy to its maximum value

$$x = \frac{2m_\mu E_{e\text{ cm}}}{m_\mu^2 + m_e^2} .$$

By angular addition to the muon polarization direction we get the electron emission angle $\theta_{e\text{ cm}}^*$ relative to the muon flight direction. The Lorentz transformation into the laboratory system with the mean velocity β_μ leads to the laboratory energy and direction

$$\begin{aligned} E_{e\text{ lab}} &= m_e \gamma_{e\text{ lab}} = \gamma_\mu (E_{e\text{ cm}} + \beta_\mu p_{e\text{ cm}} \cos \theta_{e\text{ cm}}^*) \\ \cos \theta_{e\text{ lab}} &= \frac{\gamma_\mu}{m_e \sqrt{\gamma_\mu^2 - 1}} (p_{e\text{ cm}} \cos \theta_{e\text{ cm}}^* + \beta_\mu E_{e\text{ cm}}) . \end{aligned}$$

The optional calculation of the neutrinos parameters follows an ansatz of Jarlskog [74] and uses the muon spin direction. In the cm system the angle φ between the electron direction and the muonic neutrino direction defines the quantity $\hat{\varphi}$ by

$$\hat{\varphi} = \frac{1}{2}(1 - \cos \varphi) .$$

The angle ψ describes the rotation of the plane, in which this three-body decay takes place, relative to the plane given by the muon spin and the electron emission direction. The probability distribution for a decay with the electron energy x and its emission angle $\theta_{e\text{ cm}}$ is given [75] to

$$dP \propto \frac{\hat{\varphi}}{(1 - \hat{\varphi}x)^4} \left\{ \begin{aligned} &[1 - \hat{\varphi}(2x - x^2)] - \zeta \cos \theta_{e\text{ cm}} [1 - \hat{\varphi}(2 - 2x + x^2)] \\ &- \zeta \sin \theta_{e\text{ cm}} \cos \psi 2(x - 1) \sqrt{\hat{\varphi} - \hat{\varphi}^2} \end{aligned} \right\} d\hat{\varphi} d\psi .$$

From this distribution the two angles φ and ψ are taken at random and, hence, the kinematical parameters of the neutrinos are calculated. Finally, they are transformed to the laboratory system in analogy with the electron parameters.

6.4 Kaon decays

Kaon decays produce a variety of final states consisting mostly of two or three particles. The dominant decays and their branching ratios are listed in Table 6.1.

Decay mode	Branching ratio (%)	Decay mode	Branching ratio (%)
$K^\pm \longrightarrow \mu^\pm + \nu$	63.5	$K_S^0 \longrightarrow \pi^+ + \pi^-$	68.6
$K^\pm \longrightarrow \pi^\pm + \pi^0$	21.2	$K_S^0 \longrightarrow 2\pi^0$	31.4
$K^\pm \longrightarrow \pi^\pm + \pi^\pm + \pi^\mp$	5.6	$K_L^0 \longrightarrow \pi^\pm + e^\mp + \nu$	38.7
$K^\pm \longrightarrow \pi^0 + e^\pm + \nu$	4.8	$K_L^0 \longrightarrow \pi^\pm + \mu^\mp + \nu$	27.1
$K^\pm \longrightarrow \pi^0 + \mu^\pm + \nu$	3.2	$K_L^0 \longrightarrow 3\pi^0$	21.8
$K^\pm \longrightarrow \pi^0 + \pi^0 + \pi^\pm$	1.7	$K_L^0 \longrightarrow \pi^+ + \pi^- + \pi^0$	12.4

Table 6.1: Decay modes and branching ratios for kaons.

Two-body decays

The two-body decays are isotropic in the cm system and, hence, can be treated in analogy to the charged pion decay (see section 6.2). The secondary particles are emitted back-to-back and their Lorentz factors are

$$\gamma_{1\text{ cm}} = \frac{m_K^2 + m_1^2 - m_2^2}{2m_K m_1} \quad \text{and} \quad \gamma_{2\text{ cm}} = \frac{m_K^2 - m_1^2 + m_2^2}{2m_K m_2} \quad .$$

After transformation to the laboratory system, the γ factors and angles are

$$\begin{aligned} \gamma_{i\text{ lab}} &= \gamma_K \left(\gamma_{i\text{ cm}} + \beta_K \cos \theta_{i\text{ cm}} \sqrt{\gamma_{i\text{ cm}}^2 - 1} \right) \\ \cos \theta_{i\text{ lab}} &= \frac{\gamma_K \gamma_{i\text{ lab}} - \gamma_{i\text{ cm}}}{\gamma_K \beta_K \sqrt{\gamma_{i\text{ lab}}^2 - 1}} \quad i = 1, 2 \quad . \end{aligned}$$

In the leptonic two-body kaon decay, the muon polarization direction is calculated analogously to the π^\pm decay (see section 6.2). For the optional parameter calculation of the neutrino emerging from this decay we use

$$\begin{aligned} E_{\nu\text{ lab}} &= m_K \gamma_K - m_\mu \gamma_\mu \\ \cos \theta_{\nu\text{ lab}} &= \frac{\beta_K - \cos \theta_{\mu\text{ cm}}}{1 - \beta_K \cos \theta_{\mu\text{ cm}}} \quad . \end{aligned}$$

Three-body decays

The situation for the three-body decays is treated in analogy with the neutral pion Dalitz decay (see section 6.1). The probability density function represented by the matrix element $|M|^2$ is parametrized in Ref. [76] for the decay of kaons into 3 pions by a series expansion of the form

$$|M|^2 \propto 1 + g \frac{s_3 - s_0}{m_{\pi^+}^2} + h \left(\frac{s_3 - s_0}{m_{\pi^+}^2} \right)^2 + j \frac{s_2 - s_1}{m_{\pi^+}^2} + k \left(\frac{s_2 - s_1}{m_{\pi^+}^2} \right)^2 + \dots$$

Decay mode	g	h	k
$K^\pm \longrightarrow \pi^\pm + \pi^\pm + \pi^\mp$	-0.22	0.01	-0.01
$K^\pm \longrightarrow \pi^o + \pi^o + \pi^\pm$	0.59	0.035	0.0
$K_L^o \longrightarrow \pi^+ + \pi^- + \pi^o$	0.67	0.08	0.01
$K_L^o \longrightarrow 3\pi^o$	0.0	-0.00033	0.0

Table 6.2: Coefficients of the parametrization of $K \longrightarrow 3\pi$.

Decay mode	λ_+	λ_0
$K^\pm \longrightarrow \pi^o + e^\pm + \nu_e$	0.028	0.0
$K^\pm \longrightarrow \pi^o + \mu^\pm + \nu_\mu$	0.033	0.004
$K_L^o \longrightarrow \pi^\pm + e^\mp + \nu_e$	0.03	0.0
$K_L^o \longrightarrow \pi^\pm + \mu^\mp + \nu_\mu$	0.034	0.025

Table 6.3: Coefficients of the parametrization of $K \longrightarrow \pi + \ell + \nu$.

where

$$s_i = (p_K - p_i)^2 = (m_K - m_i)^2 - 2m_K T_i \quad i = 1, 2, 3$$

$$s_0 = \frac{1}{3} \sum_i s_i = \frac{1}{3} (m_K^2 + m_1^2 + m_2^2 + m_3^2) \quad .$$

If CP invariance holds, j must be zero in good agreement with measurements. The values of the other coefficients are given in Table 6.2.

The leptonic three-body kaon decays show a probability density function that can be parametrized as described in Ref. [77]

$$|M|^2 \propto G_+^2 \left[m_K (2E_{\ell \text{ cm}} E_{\nu \text{ cm}} - m_K E'_\pi) + m_\ell^2 \left(\frac{1}{4} E'_\pi - E_{\nu \text{ cm}} \right) + H m_\ell^2 \left(E_{\nu \text{ cm}} - \frac{1}{2} E'_\pi \right) + H^2 \frac{1}{4} m_\ell^2 E'_\pi \right]$$

with m_ℓ being the mass of the lepton and

$$H = \frac{m_K^2 - m_\pi^2}{m_\pi^2} (\lambda_0 - \lambda_+) G_-$$

$$G_\pm = 1 \pm \lambda_+ \frac{m_K^2 + m_\pi^2 - 2m_K E_{\pi \text{ cm}}}{m_\pi^2}$$

$$E'_\pi = \frac{m_K^2 + m_\pi^2 - m_\ell^2}{2m_K} - E_{\pi \text{ cm}} \quad .$$

The parameters λ_+ and λ_0 that fit the data best are given in Table 6.3.

In the muonic three-body kaon decays, the muon polarization direction is calculated using the formulas given in Refs. [78, 79, 80]. In the leptonic three-body kaon decays, the kinematical parameter calculation of the emerging neutrino is optional.

6.5 η decays

The η mesons decay to two photons or – by three-body decays – to pions, occasionally accompanied by γ radiation [81]. The most frequent decay modes used in CORSIKA are listed in Table 6.4. The decay into two photons proceeds analogously to the π^0 decay as described in section 6.1, with exception of the larger decaying rest mass. The three-body decays are handled in analogy with the π^0 Dalitz decay (see section 6.1) using the Dalitz density algorithm. A constant matrix element $|M|^2$ is assumed for these decays, except for the $\eta \rightarrow \pi^+ + \pi^- + \pi^0$ decay. For the latter the matrix element $|M|^2$ is expanded to [81, 82]

$$|M|^2 \propto 1 + ay + by^2 + \dots \quad \text{with} \quad y = \frac{3T_0}{m_\eta - m_{\pi^+} - m_{\pi^-} - m_{\pi^0}} - 1$$

where T_0 is the kinetic energy of the neutral pion. The coefficients of the series expansion are adopted [82] to $a = -1.07$ and $b = 0$.

Decay mode	Branching ratio (%)
$\eta \rightarrow \gamma + \gamma$	39.13
$\eta \rightarrow 3 \pi^0$	32.09
$\eta \rightarrow \pi^+ + \pi^- + \pi^0$	23.84
$\eta \rightarrow \pi^+ + \pi^- + \gamma$	4.94

Table 6.4: Decay modes and branching ratios for η .

6.6 Strange baryon decays

All strange baryons decays are two-body decays, which are isotropic in the cm system and, hence, can be treated in analogy with the charged pion decay (see section 6.2). The decay modes and branching ratios as used in CORSIKA are listed in Table 6.5.

The decay modes of the strange anti-baryons are not listed, as they correspond to the baryons, just interchanging the particles by their anti-particles.

Decay mode	Branching ratio (%)	Decay mode	Branching ratio (%)
$\Lambda \longrightarrow p + \pi^-$	64.2	$\Xi^o \longrightarrow \Lambda + \pi^o$	100.0
$\Lambda \longrightarrow n + \pi^o$	35.8	$\Xi^- \longrightarrow \Lambda + \pi^-$	100.0
$\Sigma^+ \longrightarrow p + \pi^o$	51.64	$\Omega^- \longrightarrow \Lambda + K^-$	67.8
$\Sigma^+ \longrightarrow n + \pi^+$	48.36	$\Omega^- \longrightarrow \Xi^o + \pi^-$	23.6
$\Sigma^o \longrightarrow \Lambda + \gamma$	100.0	$\Omega^- \longrightarrow \Xi^- + \pi^o$	8.6
$\Sigma^- \longrightarrow n + \pi^-$	100.0		

Table 6.5: Decay modes and branching ratios for strange baryons.

6.7 Resonance decays

All resonances decay without tracking into two daughter particles. These decays are isotropic in the cm system and, hence, can be treated in analogy with the charged pion decay (see section 6.2). The decay modes and branching ratios for the resonance decays are derived from the combination of the quark content of the resonance with the various $q\bar{q}$ -pairs from the sea. They are listed in Table 6.6. The decay modes of the anti-baryon resonances are not listed, as they correspond to the baryon resonances, just interchanging the particles by their anti-particles.

Decay mode	Branching ratio	Decay mode	Branching ratio
$\Delta^{++} \longrightarrow p + \pi^+$	1	$K^{*o} \longrightarrow K^+ + \pi^-$	2/3
$\Delta^+ \longrightarrow p + \pi^o$	2/3	$K^{*o} \longrightarrow K_L^o + \pi^o$	1/6
$\Delta^+ \longrightarrow n + \pi^+$	1/3	$K^{*o} \longrightarrow K_S^o + \pi^o$	1/6
$\Delta^o \longrightarrow n + \pi^o$	2/3	$K^{*\pm} \longrightarrow K^\pm + \pi^o$	2/3
$\Delta^o \longrightarrow p + \pi^-$	1/3	$K^{*\pm} \longrightarrow K_L^o + \pi^\pm$	1/6
$\Delta^- \longrightarrow n + \pi^-$	1	$K^{*\pm} \longrightarrow K_S^o + \pi^\pm$	1/6
		$\bar{K}^{*o} \longrightarrow K^- + \pi^+$	2/3
$\rho^o \longrightarrow \pi^+ + \pi^-$	1	$\bar{K}^{*o} \longrightarrow K_L^o + \pi^o$	1/6
$\rho^\pm \longrightarrow \pi^\pm + \pi^o$	1	$\bar{K}^{*o} \longrightarrow K_S^o + \pi^o$	1/6

Table 6.6: Decay modes and branching ratios for resonances.

Chapter 7

Electromagnetic interactions

7.1 Muonic interactions

Muons may suffer from bremsstrahlung and e^+e^- -pair production. Both processes are negligible below 2 TeV , but become important with increasing energy. The programming of both types of interactions is taken from the detector simulation code GEANT3 [24]. The production of subthreshold electromagnetic particles is subsumed into the continuous energy loss by ionization, while only such interactions are treated explicitly, which generate electromagnetic particles above the threshold.

7.1.1 Muonic bremsstrahlung

The simulation of discrete bremsstrahlung emitted from a muon of energy E is based on Ref. [38]. The differential cross section for the emission of a bremsstrahlung photon of energy k is given by

$$\frac{d\sigma}{dv} = \frac{N}{v} \left(\frac{4}{3} - \frac{4}{3}v + v^2 \right) \Phi(\delta) \quad (7.1)$$

with the energy fraction $v = k/E$. The constant N is a normalization factor and

$$\delta = \frac{m_\mu^2}{2E} \frac{v}{1-v} \quad .$$

Dependent on the charge number Z of the traversed medium the function $\Phi(\delta)$ is calculated from

$$\Phi(\delta) = \begin{cases} \ln\left(\frac{189m_\mu}{m_e Z^{1/3}}\right) - \ln\left(\frac{189\sqrt{e}}{m_e Z^{1/3}}\delta + 1\right) & : Z \leq 10 \\ \ln\left(\frac{189m_\mu}{m_e Z^{1/3}}\right) - \ln\left(\frac{189\sqrt{e}}{m_e Z^{1/3}}\delta + 1\right) + \ln\left(\frac{2}{3}Z^{-1/3}\right) & : Z > 10 \end{cases}$$

with $e = 2.718 \dots$ Euler's constant. The energy k and hence the fraction v is limited by the photon threshold k_c and by the maximum kinematically possible value v_{max} by

$$v_c = \frac{k_c}{E} \leq v \leq \left(1 - \frac{3}{4}\sqrt{e}\frac{m_\mu}{E}Z^{1/3}\right) = v_{max} \quad .$$

Factorizing Equation 7.1 we write

$$\frac{d\sigma}{dv} = f(v)g(v) \quad (7.2)$$

with

$$f(v) = [v \ln(v_{max}/v_c)]^{-1}$$

$$g(v) = \left(1 - v + \frac{3}{4}v^2\right) \Phi(\delta)/\Phi(0) \quad .$$

The sampling of the photon energy is performed with two independent random numbers RD_1 and RD_2 distributed uniformly between 0 and 1 by sampling v from

$$v = v_c (v_{max}/v_c)^{RD_1} \quad .$$

With this fraction v the function $g(v)$ is calculated and compared with the second random number RD_2 . If $g(v) \leq RD_2$ the fraction v is accepted and the photon energy k calculated, otherwise a new set of random numbers is drawn. The energy of the muon is reduced by the photon energy, but the muon direction is unchanged. The angle between photon and muon momentum is sampled from a universal angular distribution function, which approximates the real distribution function of Ref. [83]. The photon azimuthal angle is distributed isotropically around the muon direction.

7.1.2 Muonic e^+e^- -pair production

The double differential cross section for radiating off an e^+e^- pair in a medium with charge number Z by a muon of energy E and mass m_μ is given [38] by

$$\frac{d^2\sigma}{d\nu d\rho} = \alpha^4 \frac{2}{3\pi} (Z\lambda)^2 \frac{1-\nu}{\nu} \left(\Phi_e + (m_e/m_\mu)^2 \Phi_\mu\right)$$

with the fine structure constant $\alpha = 1/137$, the electron Compton wave length $\lambda = 3.8616 \cdot 10^{-11} \text{ cm}$, the fraction of energy transferred to the pair $\nu = (E^+ + E^-)/E$ with the energies E^\pm and mass m_e of the e^\pm particles. The complete formulas for Φ_e and Φ_μ may be found in the Appendix of Ref. [38]. The quantity ρ gives the energy asymmetry of the e^+e^- -pair

$$\rho = \frac{E^+ - E^-}{E^+ + E^-} \quad .$$

The kinematic ranges of ν and ρ are defined by

$$4m_e/E = \nu_{min} \leq \nu \leq \nu_{max} = 1 - \frac{3}{4}\sqrt{e}Z^{1/3}m_\mu/E$$

$$0 = \rho_{min} \leq |\rho(\nu)| \leq \left(1 - \frac{6m_\mu^2}{E^2(1-\nu)}\right) \sqrt{1 - \frac{4m_e}{\nu E}}$$

with $e = 2.718\dots$ Euler's constant. Under the assumptions that the shapes of $\frac{d^2\sigma}{d\nu d\rho}$ and $\frac{d\sigma}{d\nu} \int d\rho \frac{d^2\sigma}{d\nu d\rho}$ do not depend on Z , the dominant contribution comes from the low ν region

$$\nu_{min} = 4m_e/E \leq \nu \leq 100\nu_{min} \quad ,$$

and that $\frac{d^2\sigma}{d\nu d\rho}$ is independent of ρ in this region, the differential cross section may be approximated [24] by

$$\frac{d\sigma}{d\nu} = \int d\rho \frac{K d^2\sigma}{d\nu d\rho} \approx \frac{1}{\nu^a} \sqrt{1 - \frac{\nu_{min}}{\nu}} \quad (7.3)$$

with $a = 2 - 0.1 \ln E$, where E is given in GeV . Analogously to Equation 7.2 we factorize Equation 7.3

$$\frac{d\sigma}{d\nu} \approx f(\nu)g(\nu) \quad \text{where} \quad f(\nu) = \frac{(a-1)}{\frac{1}{\nu^{a-1}} - \left(\frac{1}{\nu_{max}}\right)^{a-1}} \frac{1}{\nu^a}$$

is the normalized distribution between $E_c/E = \nu_c \leq \nu \leq \nu_{max}$ (with the threshold energy E_c for e^\pm) and

$$g(\nu) = \sqrt{1 - \frac{\nu_{min}}{\nu}}$$

is the rejection function. With a valid ν the maximum energy asymmetry is calculated

$$\rho_{max} = \left(1 - \frac{6m_\mu^2}{E^2(1-\nu)}\right) \sqrt{1 - \frac{4m_e}{E\nu}}$$

and the actual value of the asymmetry parameter ρ is chosen at random uniformly in the range $-\rho_{max} \leq \rho \leq +\rho_{max}$.

For the polar angle θ of the e^\pm momentum relative to the muon momentum the approximate average value $\theta = m_\mu/E$ is taken, while the azimuthal angle ϕ^+ is taken to be uniformly distributed and $\phi^- = \phi^+ + \pi$. The muon gets the final energy $E_\mu = E - E^+ - E^-$, while its original direction is kept.

7.2 Electromagnetic subshowers

Electron and photon reactions are treated with EGS4 (Electron Gamma Shower system version 4) or with the analytic NKG (Nishimura Kamata Greisen) formula. The former delivers detailed information (momentum, space coordinates, propagation time) of all electromagnetic particles, but needs extended computing times increasing linearly with the primary energy, while the latter works fast, but gives only electron densities at selected points in the detection plane.

7.2.1 Electron gamma shower program EGS4

The EGS4 option enables a full Monte Carlo simulation of the electromagnetic component of showers by calling the EGS4 package which for electrons or positrons treats annihilation, Bhabha scattering, bremsstrahlung, Møller scattering, and multiple scattering (according to Molière's theory). Gamma rays may undergo Compton scattering, e^+e^- -pair production, and photoelectric reaction. The programming of these standard interactions is well documented in Ref. [6] and therefore not described here. The direct $\mu^+\mu^-$ -pair production and the photonuclear reaction with protons and neutrons of nuclei of the atmosphere have been added. Despite their small cross sections, these two processes are essential for the muon production in gamma ray induced showers.

Photoproduction of muons and hadrons

The $\mu^+\mu^-$ pair formation is treated in full analogy with the e^+e^- pair formation replacing the electron rest mass by the muon rest mass. In the high energy limit the cross section for this process approaches

$$\sigma_{\mu^+\mu^-} = \frac{m_e^2}{m_\mu^2} \sigma_{e^+e^-}$$

and reaches $11.4 \mu b$ above $E_\gamma = 1 TeV$.

The photonuclear reaction cross section [84] of protons is shown in Fig. 7.1. Its parametrization comprises three resonances at $E_\gamma = 0.32, 0.72, \text{ and } 1.03 GeV$ superimposed on a continuum which slightly increases with energy

$$\sigma_{\gamma p} = \left(73.7s^{0.073} + 191.7/s^{0.602} \right) \sqrt{1 - s_0/s} \quad .$$

Here s and s_0 are the squared cm energy resp. pion production threshold energy in the cm system in GeV^2 and $\sigma_{\gamma p}$ is given in μb . The measurements of H1 [85] and ZEUS [86] confirm the extrapolation to higher energies. The photonuclear cross section of air is calculated from the proton cross section by multiplication with the factor $A^{0.91} = 11.44$ [84, 87]. The cross sections and branching ratios for all processes are provided in a cross section file as usual in EGS4.

In photonuclear reactions the target nucleons are treated as free particles with the assumption that only one nucleon is involved in the photonuclear process. To generate secondary particles various possibilities exist which are selected depending on the energy of the gamma ray. Below $0.4 GeV$ only one pion is generated, while in the subsequent range up to $1.4 GeV$ the chance to generate one pion decreases linearly in favour of the generation of two pions. The choice between these two possibilities is made at random. Between $1.4 GeV$ and $2 GeV$ always two pions are produced. Within the range of $2 GeV < E_\gamma < 3 GeV$ the selection between two pion generation and the HDPM option is made at random with a linearly decreasing chance for two pion generation. Above $3 GeV$ multi-particle production by the HDPM is always

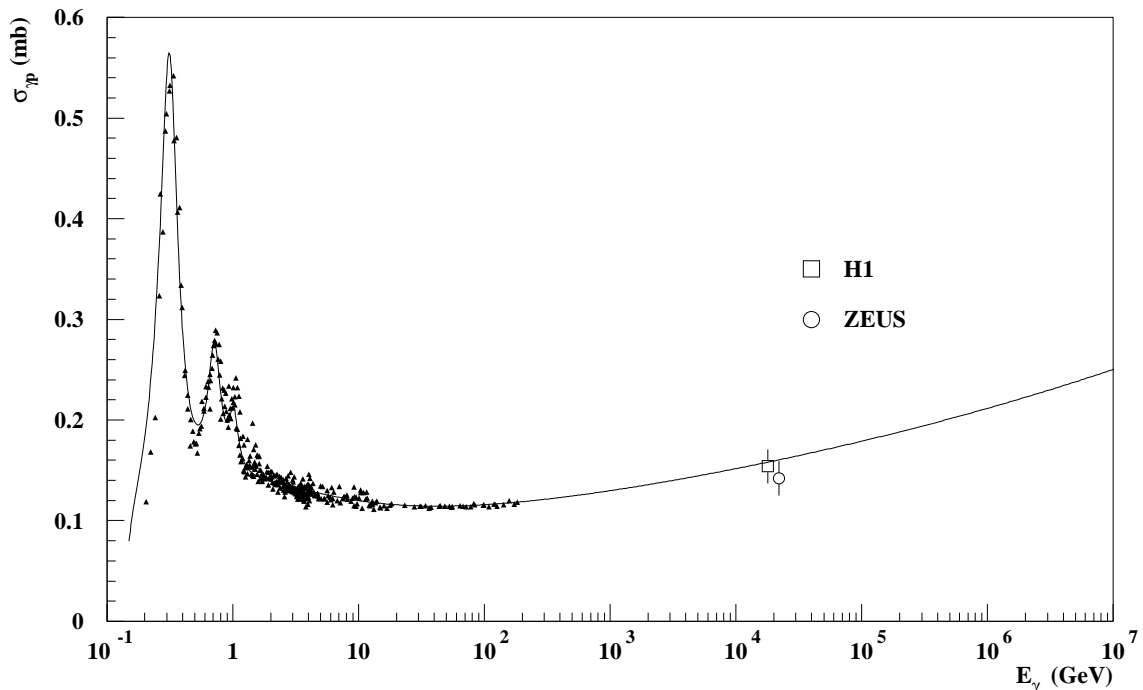


Figure 7.1: Photoproduction cross section of protons as function of energy. Data points are from Refs. [87, 85, 86].

assumed and at energies above 80 *GeV* the selected high energy hadronic interaction model is employed.

In the production of one single pion, the recoil nucleon may undergo charge exchange with 33% probability according to the decay modes of the Δ^+ and Δ^0 resonances (see Table 6.6). The pion azimuthal angle is chosen at random from a uniform distribution, while the polar angle is selected by a rejection method which produces a dipole or a quadrupole radiation characteristics depending on the energy of the gamma ray. If a charged pion is produced, these characteristics are modified to meet approximately the experimentally determined angular distributions [88].

When two pions together with a recoil nucleon are produced the particle energies are chosen to fall inside a Dalitz plot with a constant probability density. The treatment is analogous to the π^0 Dalitz decay into three secondary particles (see section 6.1). Charge exchange of the recoil nucleon is allowed giving altogether 6 exit channels respecting charge conservation. The branching ratios are listed in Table 7.1.

The production of more than two secondary particles is treated by the HDPM as described in Appendix D. In this case a neutral pion is assumed to be the interacting particle and diffraction is suppressed, but charge exchange to π^\pm is admitted. If the

Reaction mode	Branching ratio (%)	Reaction mode	Branching ratio (%)
$\gamma + p \longrightarrow \pi^o + \pi^o + p$	15	$\gamma + n \longrightarrow \pi^o + \pi^o + n$	15
$\gamma + p \longrightarrow \pi^+ + \pi^- + p$	15	$\gamma + n \longrightarrow \pi^+ + \pi^- + n$	15
$\gamma + p \longrightarrow \pi^+ + \pi^o + n$	20	$\gamma + n \longrightarrow \pi^+ + \pi^o + p$	20

Table 7.1: Branching ratios for photonuclear reactions leading to two pions.

photon energy exceeds 80 *GeV* the selected high energy interaction model is used to describe the production of secondary hadrons, and the incoming photon is replaced by a π^o or an η meson with equal chance (rsp. by a π^+ in SIBYLL).

Modifications of the standard EGS4

The essential modifications of the standard EGS4 code [6] are summarized as follows.

The barometric density dependence of air as described in section 2.4 is implemented into the particle tracking used within the EGS4 routines. Important is the path length correction of the mean free path to the next interaction according to a medium with increasing density.

The deflection of electrons and positrons in the Earth's magnetic field (see section 3.3) is calculated by an approximation only valid for small deflection angles [6]. As low energy particles at high altitude may have considerable path lengths and, hence, large deflection angles, the step size is limited to keep the deflection angle below 11.5° for each step. The propagation time (including fast renormalization of direction cosines) is calculated for the total curved path length of the particles also in the case of magnetic field deflection.

The pressure dependence of the Sternheimer correction [89] for ionization losses in air is modified. The standard EGS4 cross section files contain the continuous energy loss dE/dx of electrons and positrons for energies above 1*MeV* by ionization in gaseous matter depending on the pressure at a fixed density. The deposited energy per radiation length X_0 in air rises linearly with the logarithm of the energy (in *MeV*) as

$$dE/dx = (61.14 + 5.58 \ln E) MeV/X_0$$

until it saturates at an energy that depends on pressure. Expressed as a function of height h in *cm*, the saturation energy loss is

$$(dE/dx)_{sat} = (86.65 + 810^{-6}h) MeV/X_0 \quad .$$

This approximates the pressure dependence of the energy loss by ionization to better than 5%.

The reduction of computing time becomes important with increasing primary energy, as this time increases linearly with the energy dissipated in the atmosphere.

Therefore, the probability of electrons or gamma rays to produce a charged particle at the next observation level is estimated [90] as a function of their altitude and energy. If the probability remains below a preselected lower limit depending on shower size, this particle is discarded unless it is closer than 3 radiation lengths to the next observation level, the gamma ray energy exceeds the pion production threshold of 0.152 GeV , or the electron energy twice exceeds this threshold value. The latter conditions assure, that the production of pions which may decay into muons with large penetration depth is not suppressed. This discarding mechanism eliminates the numerous calculations of low-energy subshowers which do not contribute essentially to observable particles, thus reducing the computation time by a factor of 3. The number of lost electrons typically amounts to 3 to 5% for showers initiated by a 10^{15} eV primary and explains the difference in the electron numbers emerging from simulations with EGS4 and NKG options. However, when calculating the longitudinal shower profiles, using the Cherenkov option, or using the thinning option this discarding mechanism is switched off to keep all charged particles, as they contribute to the profile and to the emitted Cherenkov radiation or – in the case of thinning – substantially enlarge the number of arriving electrons by their higher weight.

As a second measure for reduction of computing time, the maximum step size between two multiple scattering events of electrons and positrons has been increased by a factor of 10 relative to the value of Ref. [6]. Tests [90] showed, that the influence on the lateral electron distribution is negligible for showers as would be measured by the KASCADE experiment. To keep the CORSIKA program flexible to problems, in which a more frequent treatment of the electron multiple scattering is essential – this is the case for the lateral distribution of the Cherenkov photon density initiated by gamma ray primaries with energies as low as 20 to 1000 GeV [91] – the step size increase factor may be set individually to lower values. A detailed discussion on the step length is also given in Refs. [6, 92].

To enable simulations of EAS with the highest observed energies ($\approx 10^{20} \text{ eV}$), the cross sections and branching ratios are extended also to 10^{20} eV , assuming that QED is valid. The influence of the Landau-Pomeranchuk-Migdal effect [93] is small [94] for proton induced showers even at primary energies of $5 \cdot 10^{20} \text{ eV}$. This would not hold for γ -induced showers of these energies. We consider the effect in a manner as it is done in the programs MOCCA and AIRES [95].

7.2.2 Nishimura-Kamata-Greisen option

In the NKG option the electromagnetic component of air showers is calculated by an analytical approach [96] without a full Monte Carlo simulation. The advantage of relatively modest computer time requirements for the analytical treatment is paid for with less accurate information about the electromagnetic particles. Coordinates with arrival time, location, and momenta of single electromagnetic particles cannot be obtained, but only total electron numbers at various atmospheric depths together with some parameters that give information about the general development of the

electromagnetic component of a shower. At one or two observation levels lateral electron densities are computed for a grid of points around the shower axis (see below).

Longitudinal electromagnetic shower development

The longitudinal development of the electromagnetic part of showers is obtained by calculating the total number of electrons for ≤ 10 values of atmospheric depth separated by 100 g/cm^2 down to the lowest observation level. For each subshower initiated by gamma rays (from π^0 or η decays) or by electrons of energy E , the age s_i of this subshower at each interesting level i in depth T_i (in g/cm^2) is calculated

$$s_i = \frac{3T_i/X_0}{T_i/X_0 + 2 \ln(E/E_{crit})} \quad (7.4)$$

with $E_{crit} = 82 \text{ MeV}$ being the critical energy and $X_0 = 37.1 \text{ g/cm}^2$ the radiation length in air ¹. The electron number of a subshower at level i amounts to [96]

$$N_{e_i}(E_e > 0) = \frac{0.31}{\sqrt{\ln(E/E_{crit})}} e^{(1-1.5 \ln s_i)T_i/X_0} \quad . \quad (7.5)$$

To improve Equation 7.5 to account for an energy threshold E_{thr} for the electrons, the N_{e_i} are multiplied with a correction factor

$$N_{e_i}(E_e > E_{thr}) = K N_{e_i}(E_e > 0) \quad .$$

The correction factor K has the form [16]

$$K = N_{e_i}(E_e > 0, E_{k2})/N_{e_i}(E_e > 0, E_{k1})$$

which is the quotient of electron numbers which are gained with different critical energies $E_{k1} = 0.4E_{crit}$ and $E_{k2} = E_{k1} + E_{thr}$. This correction factor amounts to 4, 10, and 30 % for threshold energies of 1, 3, and 10 MeV . At each interesting depth value, these electron numbers N_{e_i} are summed up for all subshowers.

Longitudinal age parameter

In order to describe the shower development of the overall electromagnetic or hadronic cascade in the same way as the parameter s does for individual electromagnetic subshowers, an artificial parameter, the global longitudinal age s_{long} , is introduced.

¹The Particle Data Group [97] suggests a radiation length of $X_0 = 36.7 \text{ g/cm}^2$ which would be consistent with the value used within EGS. Also a critical energy of $E_{crit} = 86 \text{ MeV}$ may be derived from this reference. These values will be adopted in the next release.

Using the age parameter s determined according to Equation 7.4, the parameters $a(s)$, $b(s)$, $C_1(s)$, and $C_2(s)$ of the NK structure functions are calculated [98, 14]

$$\begin{aligned}
a(s) &= \frac{4}{s} e^{0.915(s-1)} \\
b(s) &= 0.15 + \frac{1}{1+s} \\
C_1(s) &= \frac{a^{s/b}}{2\pi} \left(\Gamma\left(\frac{s}{b}\right) + \frac{4\Gamma\left(\frac{s+1}{b}\right)}{sa^{1/b}} \right)^{-1} \\
C_2(s) &= \frac{a^{(s+1)/b}}{2\pi} \left(\Gamma\left(\frac{s+1}{b}\right) + \frac{4\Gamma\left(\frac{s+2}{b}\right)}{sa^{1/b}} \right)^{-1} .
\end{aligned}$$

With the ratio of the coefficients $C_1(s)/C_2(s)$, the parameter R at each depth is derived by summing over all subshowers j

$$R = \frac{\sum_j (N_j C_1(s)/C_2(s))}{\sum_j N_j} .$$

with N_j the electron numbers according the improved Equation 7.5. Finally, s_{long} is defined as

$$s_{long} = \frac{\sqrt{B^2 - 4A(C - R)} - B}{2A} .$$

In this relation the coefficients A , B , and C depend on R and are given in Table 7.2.

Range of R	A	B	C
0.0191 – 0.1796	0.3109	0.2146	-0.0055
0.1796 – 0.5364	0.3667	0.1639	0.0060
0.5364 – 1.0332	0.1460	0.6317	-0.2420
1.0332 – 1.4856	-0.3376	2.0903	-1.3438

Table 7.2: Parameters of the longitudinal age formula.

Lateral electron distribution

The lateral distribution of electromagnetic showers in different materials scales well with the Molière radius $r_{mol} = 0.0212 \text{ GeV} \cdot \xi_0 / E_{crit}$. Here ξ_0 is the radiation length in cm . In the atmosphere ξ_0 varies with the density, hence, $r_{mol} = 9.6 \text{ g cm}^{-2} / \rho_{air}$. About 90% of the energy of a shower is deposited inside a cylinder around the shower axis with radius r_{mol} . In CORSIKA the electron distribution is determined for the two

lowest observation levels. The electron density ρ_e at distance r from the subshower axis is calculated according to Ref. [99]

$$\rho_e = \frac{N_e}{2\pi r_{mol}^2 s_m^2} \frac{\Gamma(4.5 - s)}{\Gamma(s)\Gamma(4.5 - 2s)} \left(\frac{r}{r_{mol}s_m}\right)^{s-2} \left(1 + \frac{r}{r_{mol}s_m}\right)^{s-4.5} \quad (7.6)$$

with the modulation function of Lagutin et al. [14, 15]

$$s_m = 0.78 - 0.21s \quad .$$

The electron densities are calculated for 80 reference points centered around the shower axis on a circular grid extending in 8 directions spaced by 45° and with 10 radial distances in each direction, covering the range from 1 m to a maximum radius which has to be specified (see Ref. [22]) in logarithmic steps. We are aware of the fact that Equation 7.6 is correct only in the Landau approximation [100] which restricts (besides others) the distance r between the considered grid point and the subshower axis to

$$\left|\frac{r}{r_{mol}}\right| > \left|\frac{E_{crit}}{E}\right| \quad .$$

This condition is violated when the subshower axis comes close to one of the grid points. The densities of all subshowers are summed up at each reference point of the grid to get the local densities of the total shower.

7.3 Cherenkov radiation

Basing on a program extension written by HEGRA collaborators [101] we have implemented an option to simulate Cherenkov radiation. This radiation is emitted, if the velocity v of charged particles – mainly electrons, but also muons and charged hadrons – exceeds the local speed of light, which is given by the local refractive index n and the vacuum speed of light c . Therefore we examine each transportation step of a charged particle for the condition

$$nv/c = n\beta > 1 \quad .$$

The refractive index n can be approximated [102] by the local density $\rho(h)$ (in g/cm^3)

$$n = 1 + 0.000283 \rho(h)/\rho(0)$$

neglecting the wavelength dependence of n . The number N_C of photons which are emitted per path length s at an angle θ_C is calculated to

$$\frac{dN_C}{ds} = 2\pi\alpha \int \frac{\sin^2 \theta_C}{\lambda^2} d\lambda$$

where the integral extends over the wavelength band, within which the Cherenkov detector is sensitive; α is the fine structure constant, and the angle θ_c relative to the charged particle direction is given by

$$\theta_c = \arccos \frac{1}{\beta n} \quad .$$

To adapt the Cherenkov simulation easily to various detector types, a wavelength band may be specified by data input.

Each charged particle path element is subdivided into smaller fractions such that, within each fractional element, the number of emitted photons is less than a predefined bunchsize. This photon bunch is treated as a whole rather than each single Cherenkov photon, thus reducing the computational effort considerably. For each photon bunch the azimuthal emission angle is taken at random, and its arrival coordinates at the detector plane are calculated.

Atmospheric absorption of the Cherenkov photons is not taken into account. But by writing the origin height of each photon bunch onto the Cherenkov output, the absorption may be introduced later when analyzing the output data.

Chapter 8

Outlook

The CORSIKA program in its present state models EAS initiated by photons, protons and nuclei up to the highest primary energies. It employs a number of theoretical models of high energy hadronic interactions which are adjusted to reproduce experimental data wherever possible. CORSIKA is a useful and flexible tool to study high energy cosmic ray interactions, to support the interpretation of EAS measurements, and to optimize the design of future cosmic ray experiments.

However, the CORSIKA program is under continuous evolution and many details of the shower development are subject to uncertainties and approximations. Wherever we are aware of such an uncertainty, we try to improve it. Some of the improvements to be implemented in the near future have already been mentioned in the text.

Unfortunately for EAS, the collider results have to be extrapolated into energy and angular regions where the interactions are supposed to change. Gluons instead of quarks become the most abundant reaction partners, heavy quarks and minijets are produced, and the collider events might look different in the forward region compared to the region with high transverse momentum where the collider detectors are located. Here theoretically founded approaches realized in different computer codes are employed. By their coupling with CORSIKA we hope to get rid of one single model, and the variations between the various models give an idea on the error of the Monte Carlo predictions of measurable quantities. We expect advances in the theories to describe high energy hadronic interactions, stimulated by the advent of new experimental data.

Appendix A

Atmospheric parameters

Layer i	Altitude h (km)	a_i (g/cm ²)	b_i (g/cm ²)	c_i (cm)
1	0 ... 4	-186.5562	1222.6562	994186.38
2	4 ... 10	-94.919	1144.9069	878153.55
3	10 ... 40	0.61289	1305.5948	636143.04
4	40 ... 100	0.0	540.1778	772170.16
5	> 100	0.01128292	1	10 ⁹

Table A.1: Parameters of the U.S. standard atmosphere.

Layer i	Altitude h (km)	a_i (g/cm ²)	b_i (g/cm ²)	c_i (cm)
1	0 ... 4	-118.1277	1173.9861	919546.
2	4 ... 10	-154.258	1205.7625	963267.92
3	10 ... 40	0.4191499	1386.7807	614315.
4	40 ... 100	$5.4094056 \cdot 10^{-4}$	555.8935	739059.6
5	> 100	0.01128292	1	10 ⁹

Table A.2: Parameters of the AT115 atmosphere (January 15, 1993).

Layer i	Altitude h (km)	a_i (g/cm^2)	b_i (g/cm^2)	c_i (cm)
1	0 ... 4	-195.837264	1240.48	933697.
2	4 ... 10	- 50.4128778	1117.85	765229.
3	10 ... 40	0.345594007	1210.9	636790.
4	40 ... 100	$5.46207 \cdot 10^{-4}$	608.2128	733793.8
5	> 100	0.01128292	1	10^9

Table A.3: Parameters of the AT223 atmosphere (February 23, 1993).

Layer i	Altitude h (km)	a_i (g/cm^2)	b_i (g/cm^2)	c_i (cm)
1	0 ... 4	-253.95047	1285.2782	1088310.
2	4 ... 10	-128.97714	1173.1616	935485.
3	10 ... 40	0.353207	1320.4561	635137.
4	40 ... 100	$5.526876 \cdot 10^{-4}$	680.6803	727312.6
5	> 100	0.01128292	1	10^9

Table A.4: Parameters of the AT511 atmosphere (May 11, 1993).

Layer i	Altitude h (km)	a_i (g/cm^2)	b_i (g/cm^2)	c_i (cm)
1	0 ... 4	-208.12899	1251.474	1032310.
2	4 ... 10	-120.26179	1173.321	925528.
3	10 ... 40	0.31167036	1307.826	645330.
4	40 ... 100	$5.591489 \cdot 10^{-4}$	763.1139	720851.4
5	> 100	0.01128292	1	10^9

Table A.5: Parameters of the AT616 atmosphere (June 16, 1993).

Layer i	Altitude h (km)	a_i (g/cm ²)	b_i (g/cm ²)	c_i (cm)
1	0 ... 4	-77.875723	1103.3362	932077.
2	4 ... 10	-214.96818	1226.5761	1109960.
3	10 ... 40	0.3721868	1382.6933	630217.
4	40 ... 100	$5.5309816 \cdot 10^{-4}$	685.6073	726901.3
5	> 100	0.01128292	1	10^9

Table A.6: Parameters of the AT822 atmosphere (August 22, 1993).

Layer i	Altitude h (km)	a_i (g/cm ²)	b_i (g/cm ²)	c_i (cm)
1	0 ... 4	-242.56651	1262.7013	1059360.
2	4 ... 10	-103.21398	1139.0249	888814.
3	10 ... 40	0.3349752	1270.2886	639902.
4	40 ... 100	$5.527485 \cdot 10^{-4}$	681.4061	727251.8
5	> 100	0.01128292	1	10^9

Table A.7: Parameters of the AT1014 atmosphere (October 14, 1993).

Layer i	Altitude h (km)	a_i (g/cm ²)	b_i (g/cm ²)	c_i (cm)
1	0 ... 4	-195.34842	1210.4	970276.
2	4 ... 10	-71.997323	1103.8629	820946.
3	10 ... 40	0.3378142	1215.3545	639074.
4	40 ... 100	$5.48224 \cdot 10^{-4}$	629.7611	731776.5
5	> 100	0.01128292	1	10^9

Table A.8: Parameters of the AT1224 atmosphere (December 24, 1993).

Altitude (m)	AT115	AT223	AT511	AT616	AT822	AT1014	AT1224	U.S. stand.
0	1055.9	1044.6	1031.3	1043.3	1025.5	1020.1	1015.1	1036.1
1000	916.8	900.9	900.7	909.9	895.6	888.9	879.2	901.3
2000	810.4	789.9	799.8	807.0	796.7	787.4	774.3	797.6
3000	715.0	690.2	707.7	713.7	707.9	695.0	679.7	703.7
4000	629.3	600.6	623.7	628.9	628.1	611.0	594.4	618.9
6000	483.0	451.0	479.3	483.8	489.8	467.5	450.6	473.9
8000	364.1	335.9	362.7	366.8	374.2	352.9	337.9	358.4

Table A.9: Air pressure values (in hPa) at low altitude for various atmospheres.

Appendix B

Muon range for horizontal showers

The disadvantage of the precise formulation of the muon range in section 4.1 is its dependence from the special atmospheric model with a density increasing exponentially along the muon path. This is no longer the case for atmospheric profiles along nearly horizontal showers with $\theta > 75^\circ$.

Starting from Equation 4.2 we consider the slowing down of the muon along its path ℓ replacing $\gamma_\mu\beta_\mu$ in Equation 4.3 resp. 4.2 by a suitable function. In a first approximation the function $\gamma_\mu(\ell)\beta_\mu(\ell)$ is expanded into a power series, omitting higher order terms:

$$\begin{aligned}\gamma_\mu(\ell)\beta_\mu(\ell) &= \gamma_{0\ \mu}\beta_{0\ \mu} + \frac{\partial(\gamma_\mu\beta_\mu)}{\partial\ell}\ell + \dots \\ &= \gamma_{0\ \mu}\beta_{0\ \mu} + \frac{\partial\gamma_\mu}{\beta_{0\ \mu}\partial\ell}\ell + \dots\end{aligned}\tag{B.1}$$

Here $\gamma_{0\ \mu}$ is the Lorentz factor and $\beta_{0\ \mu}$ the velocity at the starting point. For the ionization loss of a muon which traverses air of thickness λ we take the simple expression

$$dE_\mu = -\frac{\lambda}{\beta^2}\kappa = -\frac{\lambda\gamma^2}{\gamma^2 - 1}\kappa$$

with the energy loss by ionization of $\kappa = 2\text{ MeV g}^{-1}\text{ cm}^2$. Thus we get

$$\frac{\partial\gamma_\mu}{\partial\ell} = \frac{\partial E_\mu}{m_\mu\partial\ell} = -\frac{\kappa\rho(h_0)}{m_\mu\beta_{0\ \mu}^2}$$

where $\rho(h_0)$ gives the atmospheric density at the altitude of the muon starting point, and m_μ is the muon rest mass. Solving Equation 4.3 for the approximation of Equation B.1 leads to the individual range ℓ of the muon of

$$\ell = \frac{-\ln(RD)c\tau_\mu\gamma_{0\ \mu}\beta_{0\ \mu}}{1 - \ln(RD)c\tau_\mu\kappa\rho(h_0)/(m_\mu\beta_{0\ \mu}^3)}\tag{B.2}$$

with RD a random number distributed uniformly between 0 and 1. In contrast to section 4.1 this approximation is independent of a special atmospheric model, as the

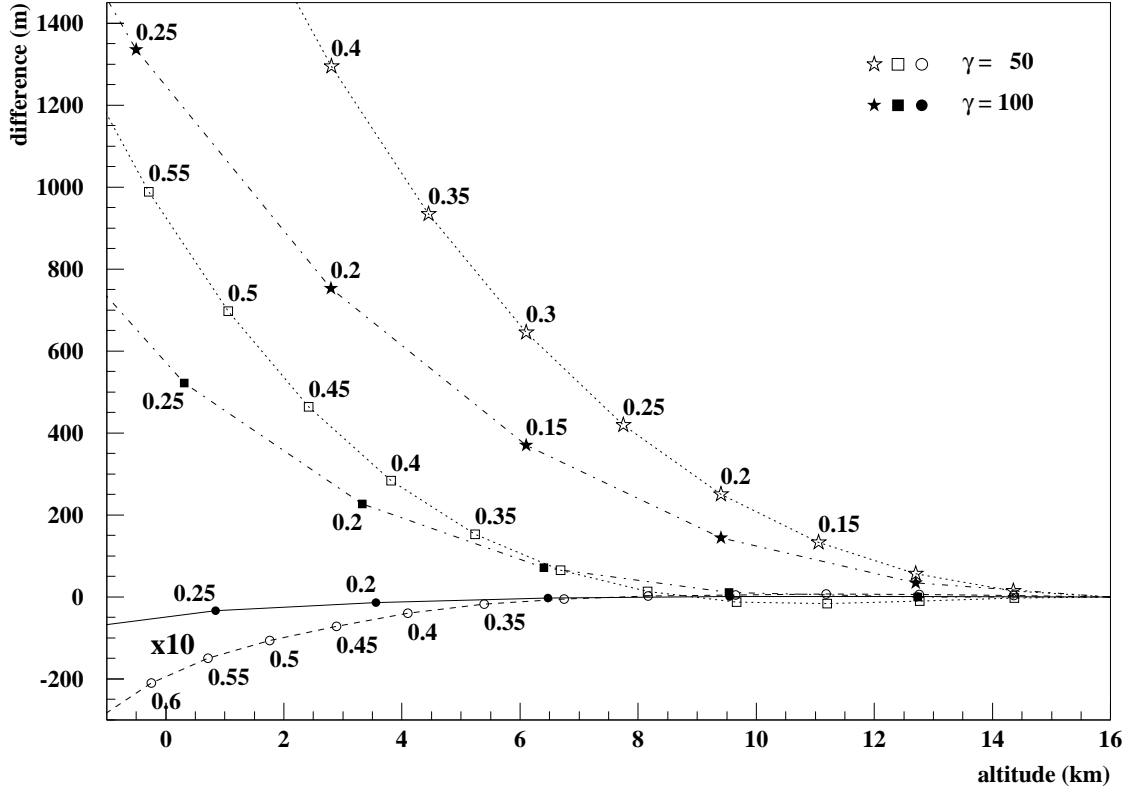


Figure B.1: Differences in the muon range calculated for vertical muons of $\gamma = 50$ (open symbols) and 100 (filled symbols) starting at 16 *km* altitude. The difference to the real penetration depth is shown for different approximations: \star Equation 4.2, \blacksquare Equation B.2, and \bullet (with $\times 10$ enlarged scale) Equation 4.5. The numbers give the fraction of the mean life time in the muon rest system.

density at the starting point may be obtained e.g. by interpolation from numerical tables. Therefore this approximation is advantageously applied in the horizontal shower version (see section 2.4), despite the limited precision.

This less precise treatment leads to an enlarged number of muons at sea level (ca. 10% for $E_\mu < 15 \text{ GeV}$) compared with the approximation of Equation 4.8. Figure B.1 shows the deviations of the different approximations from the real penetration depth of vertical muons.

Appendix C

Default cross sections

C.1 Nucleon-nucleon cross sections

This cross section is experimentally available for nucleon laboratory momenta p_{lab} up to $1000 \text{ GeV}/c$ [87] which corresponds to a center of mass (cm) energy of 44.7 GeV .

The measured nucleon-nucleon cross section [87] can well be parametrized as

$$\sigma_{n-n}(p_{lab}) = A + Bp_{lab}^N + C \ln^2 p_{lab} + D \ln p_{lab} \quad (\text{C.1})$$

where A , B , C , D , and N are free parameters of the fit. Their values are given in Table C.1. The momentum p_{lab} is given in GeV/c and σ_{n-n} is in mb .

For larger momenta the cross section is extrapolated by

$$\sigma_{n-n}(p_{lab}) = 22.01(p_{lab}^2 + m^2)^{0.0321} \quad . \quad (\text{C.2})$$

This represents an empirical fit¹ to the proton-antiproton inelastic cross section which is known up to 1.8 TeV cm energy and which is expected to be equal to the nucleon-nucleon cross section at these energies.

Employing the ISOBAR model, the measured inelastic cross section drops rapidly at low energies. Below $p_{lab} = 10 \text{ GeV}/c$ the ISOBAR model allows only elastic reactions with a constant cross section of

$$\sigma_{n-n}(p_{lab} \leq 10 \text{ GeV}/c) = 29.9 \text{ mb} \quad .$$

For antinucleons an annihilation with nucleons can occur in addition, leading to a contribution to the inelastic cross section which is parametrized in Ref. [87] by

$$\sigma_{an}(p_{lab}) = 0.532 + 63.4p_{lab}^{-0.71} \quad . \quad (\text{C.3})$$

¹The most recent issue of the Review of Particle Physics [97] gives an exponent of 0.0395. With a reduced normalization constant of 19.87 we get an identical cross section at 1000 GeV . Corresponding constants in Equation C.4 for $\pi - n$ and $K - n$ reactions are 13.25 and 11.01. These values will be adopted in the next release. This more recent approximation shifts up the HDPM curves at 10^9 GeV in Fig. 4.1 by $\approx 8\%$, in Fig. 4.3 by $\approx 18\%$, and in Fig. 4.5 by $8 - 12\%$.

Param.	$n - n$	$\pi - n$	$K - n$
A	30.9	24.3	12.3
B	-28.9	-12.3	-7.7
C	0.192	0.324	0.0326
D	-0.835	-2.44	0.738
N	-2.46	-1.91	-2.12

Table C.1: Parameters of the hadron-nucleon cross section parametrization.

From these nucleon-nucleon cross sections the nucleon-air and nucleus-air cross sections are calculated in the same manner as described in section 4.2.3 using Glauber theory.

C.2 Pion-nucleon and kaon-nucleon cross sections

Existing measurements of $\pi - n$ and $K - n$ reactions show a similar dependence on the laboratory momentum p_{lab} as nucleons. Therefore, Equation C.1 can be fitted to the measured π and K data as well. The results of such fits have been taken from Ref. [87] and are listed in Table C.1. In the momentum region above $1000 \text{ GeV}/c$ the cross sections for π and K are assumed to rise with the same momentum dependence as for nucleons. In order to get a continuous transition between the two energy regimes, only the scaling factors were modified compared to the nucleon case in Equation C.2

$$\begin{aligned}
\sigma_{\pi-n}(p_{lab}) &= 14.70(p_{lab}^2 + m^2)^{0.0321} \\
\sigma_{K-n}(p_{lab}) &= 12.17(p_{lab}^2 + m^2)^{0.0321} \quad .
\end{aligned}
\tag{C.4}$$

Again in the ISOBAR model the cross sections are taken to be constant below $p_{lab} = 5 \text{ GeV}/c$ for pions and $p_{lab} = 10 \text{ GeV}/c$ for kaons to account for elastic scattering in this energy region. The used cross section values are

$$\begin{aligned}
\sigma_{\pi-n}(p_{lab} \leq 5 \text{ GeV}/c) &= 20.64 \text{ mb} \\
\sigma_{K-n}(p_{lab} \leq 10 \text{ GeV}/c) &= 14.11 \text{ mb} \quad .
\end{aligned}$$

From these meson-nucleon cross sections the meson-air cross sections are calculated in the same manner as described in section 4.2.3 using Glauber theory.

Appendix D

HDPM

The HDPM generator describes the interactions between hadrons and nuclei at high energies and is worked out by Capdevielle [4] inspired by the Dual Parton Model (DPM) [5]. It is a phenomenological description of the interaction based on the picture that two dominant colour strings are formed between the interacting quarks of two hadrons. For instance, in a nucleon-nucleon collision, two chains (colour strings) are stretched between the fast valence di-quark of the projectile and one valence quark of the target and vice versa between the slow valence quark of the projectile and the di-quark of the target [5, 58]. The strings separate and fragment into many colour neutral secondaries that are produced around the primary quark directions. Such particle jets have been observed in many high energy physics experiments.

Recent experiments at $p\bar{p}$ colliders have improved the understanding of such reactions up to cm energies of 1.8 TeV . Unfortunately, the collider data contain mainly particles that are produced under large angles with respect to the direction of incidence (central rapidity region). But the major part of the energy escapes with the particles in the beam pipe. For the development of EAS, however, the particles emitted in forward direction are the most important ones, because they carry the energy down through the atmosphere.

In the central region, many quantities, such as the number and type of secondaries, the longitudinal and transverse momentum distributions and the spatial energy flow have been measured and correlated with each other and with the available energy. The rich data collection of collider experiments has been used to build an interaction model that reproduces the collider results as well as possible.

A difficulty arises, because air shower simulations need a description of nucleon-nucleus or even nucleus-nucleus collisions rather than nucleon-nucleon interactions. In the following sections, it is described how these interactions are modelled on the basis of the present knowledge about nucleon-nucleon reactions.

D.1 Nucleon-nucleon interactions

Number of secondaries

The average charged-particle multiplicity (including the colliding particles) in nucleon-nucleon collisions has been measured up to cm energies of 1.8 TeV . It can be parametrized [103] as a function of $s = E_{cm}^2$ (in GeV^2) by

$$\langle n_{ch} \rangle = \begin{cases} 0.57 + 0.584 \ln s + 0.127 \ln^2 s & : \quad \sqrt{s} \leq 187.5 \text{ GeV} \\ 6.89s^{0.131} - 6.55 & : \quad 187.5 \text{ GeV} < \sqrt{s} \leq 945.5 \text{ GeV} \\ 3.4s^{0.17} & : \quad 945.5 \text{ GeV} < \sqrt{s} \end{cases} . \quad (\text{D.1})$$

The actual charged-particle multiplicity n_{ch} for each event fluctuates around the average value $\langle n_{ch} \rangle$. The fluctuations follow a negative binomial distribution

$$P(n_{ch}, \langle n_{ch} \rangle, k) = \binom{n_{ch} + k - 1}{n_{ch}} \left(\frac{\langle n_{ch} \rangle / k}{1 + \langle n_{ch} \rangle / k} \right)^{n_{ch}} \left(\frac{1}{1 + \langle n_{ch} \rangle / k} \right)^k$$

where P gives the probability to obtain n_{ch} particles for the parameters $\langle n_{ch} \rangle$ and k . The dependence of k on the cm energy \sqrt{s} (in GeV) is parametrized [104] by

$$1/k = -0.104 + 0.058 \ln \sqrt{s} \quad .$$

From this distribution the actual number of charged particles n_{ch} is picked at random.

At lower energies the particle numbers are dominated by pions, therefore the average number of neutral particles $\langle n_{neu} \rangle$ produced should be around $\langle n_{ch} \rangle / 2$, and the average total multiplicity around $\langle \mathcal{N} \rangle = 1.5 \langle n_{ch} \rangle$ at low energies. At high energies, however, a larger fraction of photons than expected by $n_\gamma = 2n_{neu} = n_{ch}$ has been observed, mainly due to η meson production with subsequent decay into pions and photons.

The average number of gamma quanta $\langle n_\gamma \rangle$ adopted to reproduce this excess follows the parametrization [105]

$$\langle n_\gamma \rangle = \begin{cases} -1.27 + 0.52 \ln s + 0.148 \ln^2 s & : \quad \sqrt{s} \leq 103 \text{ GeV} \\ -18.7 + 11.55s^{0.1195} & : \quad \sqrt{s} > 103 \text{ GeV} \end{cases} . \quad (\text{D.2})$$

where $\langle n_\gamma \rangle$ is the average over many collisions, i.e. over all inclusive data. In contrast to $\langle n_\gamma \rangle$, we distinguish \bar{n}_γ as the average number of photons in collisions with the same number of charged secondaries n_{ch} . The value of \bar{n}_γ is deduced from the correlation

$$\bar{n}_\gamma = 2 + an_{ch} \quad \text{with} \quad a = \begin{cases} 0.0456 \log s + 0.464 & : \quad \sqrt{s} < 957 \text{ GeV} \\ 1.09 & : \quad \sqrt{s} \geq 957 \text{ GeV} \end{cases} .$$

We prefer this energy dependence of a compared to the constant value $a = 1.03$ given by the UA5 Collaboration [106], because it better describes the variations observed

in the energy range $200 \text{ GeV} \leq \sqrt{s} \leq 900 \text{ GeV}$. For low energies, in any case, $\langle n_{neu} \rangle$ is forced to be at least equal to $\langle n_{ch} \rangle/2$.

The actual number n_γ for a given collision is derived [107] from the observed relation between n_{ch} and n_γ in collider data [108]. For energies $\sqrt{s} > 200 \text{ GeV}$, the probability distribution of n_γ around $\bar{n}_\gamma = \langle n_\gamma \rangle z$ is described by a truncated Gaussian distribution, whose mean m and variance σ depend on $z = n_{ch}/\langle n_{ch} \rangle$ which is used as a convenient scaling variable

$$\begin{aligned} m &= \bar{n}_\gamma(0.982 - 0.376e^{-z})0.88 \\ \sigma &= m(0.147 + 2.532e^{-z})0.88 \quad . \end{aligned}$$

For $\sqrt{s} < 200 \text{ GeV}$ the fluctuations are taken to be the same as for the charged particles $n_\gamma = z\langle n_\gamma \rangle$.

The parent particles of the photons are assumed to be mainly neutral pions, but also ρ and η mesons, kaons, and hyperons can contribute to the γ component.

Particle ratios

The abundances of kaons, nucleons, Λ and Σ particles in nucleon-nucleon collisions were measured by the UA5 collaboration [109]. We adopt the UA5 parametrization [106] of the ratio of charged kaon to charged pion numbers

$$n_{K^\pm}/n_{\pi^\pm} = 0.024 + 0.0062 \ln s \quad (\text{D.3})$$

and the ratio of the number of nucleons to the number of all charged particles

$$n_N/n_{ch} = -0.008 + 0.00865 \ln s \quad . \quad (\text{D.4})$$

Λ , Σ^0 , and Σ^\pm particles are produced with the same probability and their ratio to the number of all charged particles is

$$\frac{n_\Lambda}{n_{ch}} = \frac{n_{\Sigma^0}}{n_{ch}} = \frac{n_{\Sigma^+} + n_{\Sigma^-}}{n_{ch}} = \frac{1}{3}(-0.007 + 0.0028 \ln s) \quad .$$

A noticeable contribution to photon production originates from η mesons [110]. Their abundance relative to the π^0 mesons is assumed [111] to be slightly energy dependent to

$$n_\eta/n_{\pi^0} = 0.06 + 0.006 \ln s + 0.0011 \ln^2 s \quad . \quad (\text{D.5})$$

Taking into account all these particle ratios and the specific decay modes of the particular particles, all the particle numbers of nucleons, pions, kaons, etas, and hyperons are determined to meet the previously selected charged and neutral multiplicity n_{ch} and n_γ for each single collision. It should be noted that kaons, nucleons, and hyperons are always produced as particle-antiparticle pairs.

Rapidity distribution

In hadronic reactions, jets of secondary particles are generated by the hadronizing colour strings. The kinematics of particles of a jet are described by their transverse momenta p_T and rapidities y where the latter are defined by

$$y = \frac{1}{2} \ln \frac{E + p_L}{E - p_L}$$

with E being the particle energy and p_L the longitudinal momentum. In the representation of rapidity and transverse momentum, the rapidities of the particles of a jet are approximated by a Gaussian distribution as suggested by Klar and Hüfner [112] and by inelastic hadron-hadron and lepton-hadron scattering data [113, 114]. The two principal jets of a collision are back-to-back in the center of mass and therefore positioned symmetrically around $y_{cm} = 0$ in rapidity space. The average positions of the centers of the respective Gaussians on the rapidity axis in the cm system $\langle y_{mean} \rangle$ and the average width $\langle \sigma_y \rangle$ are parametrized based on experimental data for nucleon-nucleon collisions [4]

$$\begin{aligned} \langle y_{mean} \rangle &= \pm(0.146 \ln(s - 2m_N^2) + 0.072) \\ \langle \sigma_y \rangle &= 0.12 \ln(s - 2m_N^2) + 0.18 \quad . \end{aligned} \quad (\text{D.6})$$

The rapidity of the cm system in the laboratory frame is expressed by

$$y_{cm} = \frac{1}{2} \ln \frac{E_{lab} + m_N + p_{lab}}{E_{lab} + m_N - p_{lab}}$$

with m_N being the nucleon mass and p_{lab} the nucleon momentum in the laboratory system. The amplitude of the rapidity distributions is determined by deducing the central rapidity density from data. Experimentally, however, only the pseudorapidity

$$\eta = -\ln \tan \frac{\theta}{2}$$

with θ being the cm production angle, is directly observed. The average pseudorapidity density in the central region $\langle \frac{dN}{d\eta} (\eta=0) \rangle$ as a function of the cm energy is obtained from non single diffractive data [103] as

$$\left\langle \frac{dN}{d\eta} (\eta=0) \right\rangle = \begin{cases} 0.82s^{0.107} & : \sqrt{s} \leq 680 \text{ GeV} \\ 0.64s^{0.126} & : \sqrt{s} > 680 \text{ GeV} \end{cases} \quad . \quad (\text{D.7})$$

The conversion from the measured mean pseudorapidity density in the central region to the needed mean central rapidity density is performed by

$$\left\langle \frac{dN}{dy} (y=0) \right\rangle = f_{\eta \rightarrow y} \left\langle \frac{dN}{d\eta} (\eta=0) \right\rangle$$

where $f_{\eta \rightarrow y}$ is kept constant at 1.25 for $\sqrt{s} < 19.4 \text{ GeV}$. Above, its energy dependence is deduced [115] from calculations with the DPM [58] to

$$f_{\eta \rightarrow y} = 1.28852 - 0.0065 \ln(s - 2m_N^2) \quad .$$

The central rapidity density $\frac{dN}{dy}_{(y=0)}$ eventually is calculated from the average central pseudorapidity density $\langle \frac{dN}{d\eta}_{(\eta=0)} \rangle$ in dependence from the scaling variable z as [4, 116]

$$\frac{dN}{dy}_{(y=0)} = \left\langle \frac{dN}{d\eta}_{(\eta=0)} \right\rangle f_{\eta \rightarrow y} \begin{cases} (0.487z + 0.557)^2 & : z \geq 1.5 \\ (0.702z + 0.244)^2 & : z < 1.5 \end{cases} \quad . \quad (\text{D.8})$$

The amplitude A_y of the Gaussians is deduced from the requirement that all particles belong to the Gaussians

$$\int_{-\infty}^{+\infty} \frac{dN}{dy} dy = n_{ch} \quad \text{leading to} \quad A_y = n_{ch}/(\sigma_y \sqrt{8\pi}) \quad .$$

The position of the Gaussians on the rapidity axis is now calculated such that the central rapidity density seen in semi-inclusive data is obtained by adding the two rapidity distributions in the center

$$\frac{dN}{dy}(y=0) = 2A_y e^{-y_{mean}^2/2\sigma_y^2} \quad .$$

Thus, y_{mean} is computed by

$$y_{mean} = \sigma_y \sqrt{2 \ln \left(2A_y / \frac{dN}{dy}_{(y=0)} \right)} \quad .$$

The quantity σ_y is taken to be $\langle \sigma_y \rangle$ from Equation D.6. The advantage of this procedure is to find immediately the natural position of the set of rapidities.

In case of parent particles of photons, the same procedure as for charged particles is applied to fix the position of the Gaussians as required to reproduce the theoretical central rapidity densities. Optionally a slightly modified procedure may be adopted to achieve a better agreement with experimental results [105, 117] which suggest a narrower rapidity distribution for photons. The central rapidity densities $\frac{dN}{dy}_{y=0}^\gamma$ are determined from Equations D.8 by replacing the scaling variable z by $z_\gamma = n_\gamma / \langle n_\gamma \rangle$ and multiplying it with 0.5 to account for the average ratio of neutral to charged pions and with an energy dependent factor $g(s)$ given by

$$g(s) = \begin{cases} 1 & : \sqrt{s} \leq 50 \text{ GeV} \\ 1 + 0.18 \ln(\sqrt{s}/50 \text{ GeV}) & : 50 \text{ GeV} < \sqrt{s} \leq 200 \text{ GeV} \\ 1.25 & : 200 \text{ GeV} < \sqrt{s} \end{cases} \quad .$$

As in case of charged particles, the calculations of Attallah et al. [118] suggest a more refined treatment of the conversion factor from pseudorapidity to rapidity also for the neutrals

$$f_{\eta \rightarrow y}^\gamma = \frac{\left\langle \frac{dN^\gamma}{dy} \right\rangle_{(y=0)}}{\left\langle \frac{dN^\gamma}{d\eta} \right\rangle_{(\eta=0)}} = \begin{cases} 1.1 & : \sqrt{s} \leq 19.4 \text{ GeV} \\ 1.33 - 0.0391 \ln(s - 2m_N^2) & : 19.4 \text{ GeV} < \sqrt{s} \leq 900 \text{ GeV} \\ 0.8 & : 900 \text{ GeV} < \sqrt{s} \end{cases}$$

to take into account UA5 results [105].

For each particle its rapidity y_i in the cm system is chosen from the appropriate Gaussian distribution at random.

Transverse momentum of the secondaries

The transverse momentum distribution of secondaries in nucleon-nucleon collisions is well described [119] by

$$\frac{d^2N}{dp_x dp_y} \propto \left(\frac{p_0}{p_0 + p_T} \right)^n \quad . \quad (\text{D.9})$$

With $p_T = \sqrt{p_x^2 + p_y^2}$ one obtains the probability density function

$$\frac{dN}{dp_T} = \frac{(n-1)(n-2)}{p_0^2} \left(\frac{p_0}{p_0 + p_T} \right)^n p_T \quad (\text{D.10})$$

where $p_0 = 1.3 \text{ GeV}/c$ for pions and the parameter n depends on the central pseudorapidity density $\frac{dN}{d\eta} \Big|_{(|\eta| < D)} = \rho_{|\eta| < D}$ of charged secondaries as [120]

$$n = 7.4 + 3.67/\rho_{|\eta| < D}^{0.435} \quad .$$

The pseudorapidity density $\rho_{|\eta| < D}$ is calculated from the central region of width $2D$ with

$$D = 0.67(2.95 + 0.0302 \ln s) \quad .$$

For collisions with $\sqrt{s} > 500 \text{ GeV}$ a recent analysis [121] of the UA1 (minimum bias) experiment indicates a new correlation of $\langle p_T \rangle$ with the central pseudorapidity density $\rho_{|\eta| < D}$. For fixed $p_0 = 1.3 \text{ GeV}/c$ this dependence is parametrized [122] to

$$\langle p_T \rangle = \begin{cases} 0.0033(\rho_{|\eta| < D} - 1.56)^2 + 0.406 & : \rho_{|\eta| < D} < 3 \\ 0.0109\rho_{|\eta| < D} + 0.383 & : \rho_{|\eta| < D} \geq 3 \end{cases} \quad .$$

To sample p_T from Equation D.9 for $E_{cm} > 500 \text{ GeV}$ the inverse integral method is applied which leads to a transcendent equation of the form

$$\frac{RD}{n-1} \left(\frac{p_T}{p_0} + 1 \right)^{n-1} + \frac{1}{n-1} - \frac{p_T}{p_0} = 0 \quad . \quad (\text{D.11})$$

RD is a random number uniformly distributed between 0 and 1, the parameter n is connected with $\langle p_T \rangle$ by

$$n = \frac{2.64}{\langle p_T \rangle} + 3 \quad .$$

Within CORSIKA Equation D.11 is solved by a rejection method.

According to these distributions, the transverse momenta are determined for secondary pions only. As there is experimental evidence [123] on differences between the transverse momentum distributions of secondary pions, kaons, nucleons, η mesons, and strange baryons, this is accounted for by applying energy dependent correction factors $\langle p_T^K \rangle / \langle p_T^\pi \rangle$, $\langle p_T^N \rangle / \langle p_T^\pi \rangle$, $\langle p_T^\eta \rangle / \langle p_T^\pi \rangle$, and $\langle p_T^{sb} \rangle / \langle p_T^\pi \rangle$ with

$$\begin{aligned} \langle p_T^\pi \rangle(s) &= \begin{cases} 0.3 + 0.00627 \ln s & : E_{cm} < 132 \text{ GeV} \\ (0.442 + 0.0163 \ln s)^2 & : E_{cm} \geq 132 \text{ GeV} \end{cases} \\ \langle p_T^K \rangle(s) &= \begin{cases} 0.381 + 0.00797 \ln s & : E_{cm} < 131 \text{ GeV} \\ (0.403 + 0.0281 \ln s)^2 & : E_{cm} \geq 131 \text{ GeV} \end{cases} \\ \langle p_T^N \rangle(s) &= \begin{cases} 0.417 + 0.00872 \ln s & : E_{cm} < 102 \text{ GeV} \\ (0.390 + 0.0341 \ln s)^2 & : E_{cm} \geq 102 \text{ GeV} \end{cases} \\ \langle p_T^\eta \rangle(s) &= 0.88 \langle p_T^K \rangle + 0.12 \langle p_T^N \rangle \\ \langle p_T^{sb} \rangle(s) &= 1.45 \langle p_T^N \rangle - 0.45 \langle p_T^K \rangle \quad . \end{aligned}$$

A slight inconsistency should be noted. Instead of using the energy dependence of $\langle p_T \rangle$ from Equation D.1 the $\ln s$ parametrization is used in the correction factors only. The advantage of this method is to follow closely the correlation of $\langle p_T \rangle$ with the average central rapidity density.

The sum $S_{p_T} = \sum_i^{\mathcal{N}} p_{T,i}$ of the transverse momenta of all secondaries is calculated and the p_T values of the particles are reduced by S_{p_T} / \mathcal{N} to fulfill transverse momentum conservation.

Energy of secondaries and leading particles

The laboratory energy of particle i is calculated according to

$$E_i = \sqrt{p_{T,i}^2 + m_i^2} \cosh(y_i + y_{cm})$$

for all but two particles. These extra particles are regarded as the remainder of the collision partners, and their energies are treated in a differing manner. For the ‘anti-leader’ (the remnant of the participating target nucleon) the energy is taken at random from a Feynman x distribution, which is parametrized [124] within three regions as

$$\frac{dN}{dx_F} = \begin{cases} cx_F & : 0 \leq x_F < x_1 \\ cx_1 & : x_1 \leq x_F < x_2 \\ cx_1 e^{-\alpha(x_F - x_2)} & : x_2 \leq x_F < 1 \end{cases}$$

	$\sqrt{s} < 13.8 \text{ GeV}$	$13.8 \text{ GeV} \leq \sqrt{s} < 5580 \text{ GeV}$	$5580 \text{ GeV} \leq \sqrt{s}$
x_1	0.2	$0.71 + 0.00543 \ln(s - 2m_N^2)$	0.265
x_2	0.65	$0.8175 - 0.032 \ln(s - 2m_N^2)$	0.265
α	1.265	$1.14 + 0.022 \ln(s - 2m_N^2)$	$1.14 + 0.022 \ln(s - 2m_N^2)$

Table D.1: Energy dependence of x_1 , x_2 , and α .

where c is a constant to normalize the distribution. The boundaries x_1 and x_2 and the parameter α depend on energy as given in Table D.1.

The ‘leader’ (residue of the projectile) gets the remainder of energy after subtraction of the energies of anti-leader and all secondaries. In case this is not possible, because there is not enough energy left, the particle generation is repeated with a new set of rapidities.

In high energy collisions, about 50% of the cm energy is carried away by secondary particles, which is usually noted as an inelasticity parameter $k \approx 0.5$. This value is reproduced rather well by the HDPM generator without any additional constraint. By attributing the remaining energy to the ‘leader’ particle, this will in general be the most energetic one.

Two further alternatives have been proposed in literature to determine the leading particle rapidity. Alner et al. [106] attribute the largest of the randomly selected rapidities of the secondaries to the leading particle. The second alternative picks the leading particle rapidity from a separate distribution resulting from DPM calculations [125] for the valence quarks recombined in the final state. There is no decisive argument yet in favor of one of the three treatments.

To balance energy and longitudinal momenta of leader, anti-leader, and of all secondaries simultaneously, all rapidities are slightly modified using the algorithm of Jadach [126], which delivers the corrected rapidity $y_{c\ i}$ of particle i to

$$y_{c\ i} = A + By_i \quad .$$

The size of A is predominantly determined by longitudinal momentum conservation and B by energy conservation; both parameters are approximated by an iterative adjustment procedure for each collision. The transverse momentum of the leading particles is chosen analogously to the secondary particles, depending on the particle type.

Charge exchange and resonance formation

The leading particle after the collision is correlated with the primary incoming particle due to the fact that the fast spectator quarks of the interaction move almost with their initial velocity and most likely form the fastest secondary particle together with an additional quark. This picture limits the possible types of the leading particles

leader		other pion		leader		other pion
π^-	+	π^o	\longrightarrow	π^o	+	π^-
π^+	+	π^o	\longrightarrow	π^o	+	π^+
π^o	+	π^-	\longrightarrow	π^-	+	π^o
π^o	+	π^+	\longrightarrow	π^+	+	π^o
K^-	+	π^o	\longrightarrow	$K_{L/S}^o$	+	π^-
K^+	+	π^o	\longrightarrow	$K_{L/S}^o$	+	π^+
$K_{L/S}^o$	+	π^+	\longrightarrow	K^+	+	π^o
$K_{L/S}^o$	+	π^-	\longrightarrow	K^-	+	π^o
p	+	π^o	\longrightarrow	n	+	π^+
n	+	π^+	\longrightarrow	p	+	π^o
\bar{p}	+	π^o	\longrightarrow	\bar{n}	+	π^-
\bar{n}	+	π^-	\longrightarrow	\bar{p}	+	π^o

Table D.2: Charge exchange of leading particles. To conserve charge, another pion has also to change its charge state.

that can appear for a given primary. The leading particle may be of the same type as the incoming one, undergo charge exchange, or may be excited to a resonance state. For reasons of charge conservation the charge of a further (secondary) pion is changed in both processes. The possible charge exchange and resonance formation combinations which are taken into account are listed in Table D.2 and Table D.3. If more than one possibility exists for a leading particle to perform charge exchange or resonance formation, a random selection is made respecting phase space considerations. After charge exchange or resonance production the number of positive, negative, and neutral pions is adjusted in a manner, that the total charge involved in the collision is conserved, and that after decay of resonances the number of charged and neutral pions approaches the experimentally observed values as close as possible.

The probability for charge exchange varies with energy as

$$P_{ex} = \begin{cases} 0.10 & : & \sqrt{s} \leq 19.4 \text{ GeV} \\ 0.10 + 0.0345 \ln(E_{lab}/200 \text{ GeV}) & : & 19.4 \text{ GeV} < \sqrt{s} \leq 105 \text{ GeV} \\ 0.45 - 0.0537 \ln(E_{lab}/200 \text{ GeV}) & : & 105 \text{ GeV} < \sqrt{s} \leq 969 \text{ GeV} \\ 0.03 & : & 969 \text{ GeV} < \sqrt{s} \end{cases} \quad (\text{D.12})$$

and similarly the probability for resonance formation is taken to

$$P_{rf} = \begin{cases} 0.35 & : & \sqrt{s} \leq 105 \text{ GeV} \\ 0.08819 \ln(E_{lab}/200 \text{ GeV}) & : & 105 \text{ GeV} < \sqrt{s} \leq 969 \text{ GeV} \\ 0.69 & : & 969 \text{ GeV} < \sqrt{s} \end{cases} \quad (\text{D.13})$$

leader		secondary pion		resonance	branching ratio
π^-	+	π^o	\longrightarrow	ρ^-	1/2
π^-	+	π^+	\longrightarrow	ρ^o	1/2
π^+	+	π^-	\longrightarrow	ρ^o	1/2
π^+	+	π^o	\longrightarrow	ρ^+	1/2
K^-	+	π^o	\longrightarrow	K^{*-}	1/2
K^-	+	π^+	\longrightarrow	\bar{K}^{*o}	1/2
K^+	+	π^o	\longrightarrow	K^{*+}	1/2
K^+	+	π^-	\longrightarrow	K^{*o}	1/2
$K_{L/S}^o$	+	π^-	\longrightarrow	K^{*-}	1/4
$K_{L/S}^o$	+	π^+	\longrightarrow	K^{*+}	1/4
$K_{L/S}^o$	+	π^o	\longrightarrow	K^{*o}	1/4
$K_{L/S}^o$	+	π^o	\longrightarrow	\bar{K}^{*o}	1/4
p	+	π^+	\longrightarrow	Δ^{++}	1/2
p	+	π^o	\longrightarrow	Δ^+	1/3
p	+	π^-	\longrightarrow	Δ^o	1/6
n	+	π^+	\longrightarrow	Δ^+	1/6
n	+	π^o	\longrightarrow	Δ^o	1/3
n	+	π^-	\longrightarrow	Δ^-	1/2
\bar{p}	+	π^-	\longrightarrow	$\bar{\Delta}^{--}$	1/2
\bar{p}	+	π^o	\longrightarrow	$\bar{\Delta}^-$	1/3
\bar{p}	+	π^+	\longrightarrow	$\bar{\Delta}^o$	1/6
\bar{n}	+	π^-	\longrightarrow	$\bar{\Delta}^-$	1/6
\bar{n}	+	π^o	\longrightarrow	$\bar{\Delta}^o$	1/3
\bar{n}	+	π^+	\longrightarrow	$\bar{\Delta}^+$	1/2

Table D.3: Resonance formation of leading particles. To preserve the final number of pions, another pion must be subsumed into the resonance.

Both the ‘leader’ and the ‘anti-leader’ may independently undergo charge exchange or resonance formation with the same probabilities. The charge exchange and resonance formation reactions may be suppressed by a control flag.

The resonance formation of the leading particles involves important consequences for the hadron cascading in EAS [127, 128] due to subsequent decay or modified penetration depth in case of decay to the electromagnetic channel.

Diffractive processes

Most of the particles do not experience completely central collisions. In peripheral collisions it may happen that the projectile is just excited by a rather small energy and momentum transfer from a target nucleon. The excited projectile subsequently decays and forms secondary particles. Such interactions are called diffractive processes. Their topology is different from the non-diffractive events, mainly due to the reduced amount of energy E_{SD} that is available for production of secondary particles. As suggested by experimental data [129], a fraction of 15% of all interactions is assumed to be diffractive in the present version of the program. Strictly speaking, the ratio of diffractive to total cross section is slightly energy dependent following the parametrization by [58]

$$\sigma_{SD} = (1.77 \ln^{0.7} s - 2.38) \text{ mb} \quad .$$

In principle, diffractive interactions are treated in the same way as non-diffractive processes, with the following differences:

First, experimental results [130] and theoretical predictions [131] indicate the excitation energy E_{SD} to follow

$$\frac{d\sigma_{SD}}{d(E_{SD}^2/s)} \propto \frac{1}{E_{SD}^2/s} \quad .$$

E_{SD} must be large enough to produce at least one additional pion, but is limited to at maximum 5% of the cm energy.

Second, the position and width of the Gaussians in rapidity space are calculated as indicated in Equation D.6, however, replacing s by $s_{SD} = E_{SD}^2$ and shifting the zero point by

$$y_{0 \text{ } SD} = y_{cm} \pm \ln(E_{cm}/E_{SD})$$

with the positive sign for projectile diffraction and negative sign for target diffraction. With the same substitution for s the excess of photons from decaying secondaries is described as explained in Equation D.2, and the particle ratios of kaons and nucleons to pions are calculated following Equations D.3 and D.4.

Third, hyperon production in diffractive interactions is neglected, while η mesons are produced according to Equation D.5.

The average central pseudorapidity density is taken in analogy to Equation D.7 to

$$\langle \rho_{\eta=0} \rangle = 0.82 E_{SD}^{0.214}$$

neglecting the parametrization for energies above 680 GeV. The average number of charged particles varies with the energy in the same way as for the non-diffractive case [111, 132]. Therefore, we adopt the parametrization of Equation D.1 and replace s by s_{SD} .

With these parametrizations the same procedure is followed to generate secondaries, their rapidities and transverse momenta. The energy of the diffracted leading

particle is taken from the Gaussian shaped rapidity distributions at random as for the secondaries, while the rapidity of the non-diffracting leading particle is calculated from the primary energy reduced by the mass of the diffracting system. Charge exchange and resonance formation is only considered for the diffracting collision partner, replacing s by s_{SD} in Equations D.12 and D.13. Due to the smaller amount of energy available the overall number of secondaries is smaller. Energy and momentum conservation is accomplished also by the Jadach filtering method, as described above.

D.2 Nucleon-nucleus interactions

In an EAS the incoming particle does not collide with free nucleons but with nuclei of the air target. Consequently, the interaction model has to be adapted to this situation. Since the nucleon-nucleon interactions are experimentally well studied, we try to construct the nucleon-nucleus interaction basically in terms of the nucleon-nucleon interaction.

The treatment of nucleon-nucleus or nucleus-nucleus interactions starts with the identification of the type of target nucleus. Therefore, the relative contributions of the various air nuclei to the total inelastic cross section have been calculated and the choice is made at random according to these contributions.

When a high energy nucleon hits an air nucleus, it does not interact with the whole nucleus, but with a few target nucleons only. The number n_T of ('wounded') target nucleons hit by the projectile can be determined in two different manners. Either, a parametrization of $\langle n_T \rangle$ depending on the target mass number A_{target} and the square of the cm energy s is used [4]

$$\langle n_T \rangle = (0.56 + 0.0236 \ln(s - 1.76)) A_{target}^{0.31} \quad (\text{D.14})$$

neglecting the fluctuations of n_T around its mean value. In the second option n_T is explicitly selected according to its probability distribution [133] which is obtained by Glauber calculations.

In case of diffractive interactions, we either set $n_T = 1$ or calculate it according to Equation D.14 with s being replaced by s_{SD} .

Thus, the primary particle is assumed to interact with n_T nucleons of the target successively. Obviously the multiple interactions in one nucleus are not independent of each other. Our approach accounts for the multiple interactions in the target by several corrections based on an analysis by Klar and Hüfner [112]. The main one is the production of additional secondaries, the target excess. This excess was measured by observing the extra negative particles Δn_- from nucleon-nucleus collisions and was parametrized [112] as

$$\langle \Delta n_- \rangle = \begin{cases} 0.285(n_T - 1)\langle n_{ch} \rangle & : E_{cm} \leq 137 \text{ GeV} \\ 0.25(n_T - 1)\langle n_{ch} \rangle & : E_{cm} > 137 \text{ GeV} \end{cases} .$$

The neutral excess is then $\langle \Delta n_{neu} \rangle = \langle \Delta n_- \rangle$ and the number of additional charged particles from the target excess is $\langle \Delta n_{ch} \rangle = 2\langle \Delta n_- \rangle$. The additional particles originate from a third string which is modelled by a third Gaussian distribution in rapidity space.

When choosing the energies of the particles from the target excess, the rapidities are taken at random from the third Gaussian. The particle types of the target excess are determined following the same ratios as are used for the other secondaries.

The parametrization of position y_m and width σ of this Gaussian, depending on the number of reacting target nucleons n_T , is given [4] by

$$\begin{aligned} y_m &= -3 + 2.575e^{-0.082n_T} \\ \sigma &= 1.23 + 0.079 \ln n_T \quad . \end{aligned}$$

The final position of the third Gaussian is chosen in full analogy with the procedure described above such that the particle excess in the center of rapidity equals the observed values $\rho_{y=0}^3$ with [134]

$$\rho_{y=0}^3 = \rho_{y=0} \frac{n_T - 1}{2} \quad .$$

The target excess lies at negative rapidity values in all cases.

According to HELIOS results [135] we assume the ratio of diffractive to total inelastic cross section to be the same for nucleon-nucleon and nucleon-nucleus collisions.

D.3 Pion-nucleus and kaon-nucleus interactions

The interactions of pions and kaons with a nucleus are simulated in strict analogy with the nucleon-nucleus interaction. Only for the calculation of the available cm energy and the determination of the number of target nucleons involved in the interaction process, the different masses and cross sections of pions and kaons are taken into account. All other features described in the nucleon case are the same for pions and kaons.

D.4 Nucleus-nucleus interactions

The probability of n_P projectile nucleons interacting and the probability of a projectile nucleon hitting n_T target nucleons are evaluated by Glauber calculations [45, 133] and kept as tables (see section 4.2.3). The actual probabilities are interpolated from these tables in analogy with the cross section values and used for a random selection of n_P and n_T . The further reaction is now regarded as a superposition of n_P nucleon-nucleus reactions which are simulated as described in section D.2. The ratio

of interacting protons and neutrons is assumed to be equal to the ratio in the parent nucleus.

The treatment of the non-interacting nucleons of the projectile (spectators) may be selected to ‘total fragmentation’, ‘no fragmentation’, or evaporation. For the evaporation treatment three options are available which differ only in the selection of the transverse momenta (see section 5.3).

Acknowledgements

We would like to thank all colleagues in the various laboratories around the world who have contributed to the development of the CORSIKA program by reporting their problems, experience, suggestions, and detected errors.

Special thanks go to the authors of the various hadronic interaction programs R.S. Fletcher, T.K. Gaisser, N.N. Kalmykov, P. Lipari, S.S. Ostapchenko, J. Ranft, and K. Werner for the permission to use their programs and for many helpful discussions and hints in coupling their codes with CORSIKA.

The contribution of the Cherenkov routines by the HEGRA collaborators F. Arqueros, J. Cortina, S. Martinez (Madrid), and M. Rozanska (Cracow) is acknowledged as well as the design of some system routines by G. Trinchero (Torino), by D. Horn and M. Raabe (Hamburg). We are indebted to C. Pryke (Chicago) for many communications, which helped us to tune CORSIKA to the highest energies.

We especially thank our Karlsruhe colleagues H.J. Gils, J. Oehlschläger, and H. Rebel, who regularly discussed with us all the problems arising in the simulations with CORSIKA.

Bibliography

- [1] P. Doll et al., The Karlsruhe Cosmic Ray Project KASCADE, Report **KfK 4686** (1990), Kernforschungszentrum Karlsruhe; *Nucl. Phys. B (Proc. Suppl.)* **14A** (1990) 336
- [2] H.O. Klages for the KASCADE Collaboration, *Nucl. Phys. B (Proc. Suppl.)* **52B** (1997) 92; *Proc. 25th Int. Cosmic Ray Conf.*, Durban, **6** (1997) 141
- [3] P.K.F. Grieder, Report **INS–J125** (1970), Inst. for Nuclear Studies, Univ. of Tokyo; P.K.F. Grieder, *Proc. 16th Int. Cosmic Ray Conf.*, Kyoto, **9** (1979) 161
- [4] J.N. Capdevielle, *J. Phys. G: Nucl. Part. Phys.* **15** (1989) 909
- [5] A. Capella and J. Tran Thanh Van, *Phys. Lett.* **B93** (1980) 146
- [6] W.R. Nelson, H. Hirayama and D.W.O. Rogers, Report **SLAC 265** (1985), Stanford Linear Accelerator Center
- [7] K. Werner, *Phys. Rep.* **232** (1993) 87
- [8] N.N. Kalmykov, S.S. Ostapchenko, *Yad. Fiz.* **56** (1993) 105; *Phys. At. Nucl.* **56**(3) (1993) 346; N.N. Kalmykov, S.S. Ostapchenko and A.I. Pavlov, *Bull. Russ. Acad. Sci. (Physics)* **58** (1994) 1966
- [9] J. Ranft, *Phys. Rev.* **D51** (1995) 64
- [10] R.S. Fletcher, T.K. Gaisser, P. Lipari and T. Stanev, *Phys. Rev.* **D50** (1994) 5710
- [11] J. Engel, T.K. Gaisser, P. Lipari and T. Stanev, *Phys. Rev.* **D46** (1992) 5013
- [12] H. Fesefeldt, Report **PITHA–85/02** (1985), RWTH Aachen
- [13] S.S. Ostapchenko, T. Thouw and K. Werner, *Nucl. Phys. B (Proc. Suppl.)* **52B** (1997) 3; K. Werner, private communication (1997)
- [14] J.N. Capdevielle and J. Gawin, *J. Phys. G: Nucl. Part. Phys.* **8** (1982) 1317
- [15] A.A. Lagutin et al., *Proc. 16th Int. Cosmic Ray Conf.*, Kyoto, **7** (1979) 18

- [16] J.N. Capdevielle, KASCADE Collaboration, *Proc. 22nd Int. Cosmic Ray Conf.*, Dublin, **4** (1991) 405
- [17] *Proc. 24th Int. Cosmic Ray Conf.*, Rome, (1995)
- [18] *Proc. 25th Int. Cosmic Ray Conf.*, Durban, (1997)
- [19] J. Knapp et al., *Proc. 24th Int. Cosmic Ray Conf.*, Rome, **1** (1995) 403
- [20] D. Heck for the KASCADE Collaboration, *Proc. 25th Int. Cosmic Ray Conf.*, Durban, **6** (1997) 245
- [21] J.N. Capdevielle et al., Report **KfK 4998** (1992), Kernforschungszentrum Karlsruhe
- [22] J. Knapp and D. Heck, Report **KfK 5196B** (1993), Kernforschungszentrum Karlsruhe; for an up-to-date version see <http://www-ik3.fzk.de/~heck/corsika/>
- [23] O. C. Allkofer and P. K. F. Grieder, Cosmic Rays on Earth, in: *Physics Data 25/1*, H. Behrens and G. Ebel eds. (Fachinformationszentrum Karlsruhe, Germany, 1983) chpt. 1.1.2
- [24] R. Brun et al., GEANT3, Report **CERN DD/EE/84-1** (1987), CERN, Geneva
- [25] M. Aguilar-Benitez et al. (Particle Data Group), *Phys. Rev.* **D45** (1992) II, 6; VIII, 40
- [26] P.E. Hauenstein, *Atomic Nucl. Data Tables* **39** (1988) 290 (The values of A.H. Wapstra, G. Audi, R. Hoekstra are taken.)
- [27] Handbook of Chemistry and Physics, 67th Edition, R.C. Weast ed. (The Chemical Rubber Co., Cleveland, 1986) F141
- [28] J. Linsley, private communication by M. Hillas (1988)
- [29] H. Ulrich, Diploma thesis University Karlsruhe (1997) (unpublished)
- [30] G. Marsaglia and A. Zaman, Report **FSU-SCRI-87-50** (1987), Florida State University
- [31] F. James, Report **CERN DD/88/22** (1988), CERN, Geneva
- [32] R.M. Sternheimer, M.J. Berger and S.M. Seltzer, *Atomic Nucl. Data Tables* **30** (1984) 261
- [33] G.Z. Molière, *Z. Naturforsch.* **2a** (1947) 133; *Z. Naturforsch.* **3a** (1948) 78
- [34] H.A. Bethe, *Phys. Rev.* **89** (1953) 1256

- [35] B. Rossi, High Energy Particles (Prentice Hall, Englewood Cliffs, New Jersey, 1952)
- [36] <http://www.ngdc.noaa.gov/seg/potfld/geomag.html>
- [37] M. Hillas, *Nucl. Phys. B (Proc. Suppl.)* **52B** (1997) 29
- [38] W. Lohmann, R. Kopp and R. Voss, Report **CERN 85-03** (1985), CERN, Geneva
- [39] G. Schatz and D. Heck, internal report, unpublished (1995)
- [40] H.H. Mielke et al., *J. Phys. G: Nucl. Part. Phys.* **20** (1994) 637
- [41] G.B. Yodh et al., *Phys. Rev.* **D27** (1983) 1183
- [42] T.K. Gaisser et al., *Phys. Rev.* **D36** (1987) 13503
- [43] R.M. Baltrusaitis et al., *Phys. Rev. Lett.* **52** (1993) 1380
- [44] M. Honda et al., *Phys. Rev. Lett.* **70** (1993) 525
- [45] R.J. Glauber and G. Matthiae, *Nucl. Phys.* **B21** (1970) 135
- [46] K.G. Boreskov and A.B. Kaidalov, *Sov. J. Nucl. Phys.* **48** (1988) 367
- [47] H. de Vries et al., *Atomic Nucl. Data Tables* **36** (1987) 495
- [48] J. Knapp, D. Heck and G. Schatz, Report **FZKA 5828** (1996), Forschungszentrum Karlsruhe
- [49] J. Knapp, Report **FZKA 5970** (1997), Forschungszentrum Karlsruhe
- [50] J. Knapp et al., to be published
- [51] M. Adamus et al., EHS–NA22 Collaboration, *Z. Phys.* **C39** (1988) 311
- [52] D.W. Duke and J.F. Owens, *Phys. Rev.* **D30** (1984) 49
- [53] A.B. Kaidalov and K.A. Ter-Martirosyan, *Sov. J. Nucl. Phys.* **39** (1984) 979
- [54] A.B. Kaidalov, K.A. Ter-Martirosyan and Yu.M. Shabelsky, *Sov. J. Nucl. Phys.* **43** (1986) 822
- [55] B. Andersson et al., *Phys. Rep.* **97** (1983) 31
- [56] T. Sjöstrand, *Comp. Phys. Comm.* **39** (1986) 347
- [57] N.N. Kalmykov and S.S. Ostapchenko, *Sov. J. Nucl. Phys.* **50** (1989) 315

- [58] P. Aurenche, F.W. Bopp, A. Capella, J. Kwiecinski, M. Maire, J. Ranft and J. Tran Thanh Van, *Phys. Rev.* **D45** (1992) 92
- [59] F.W. Bopp, D. Petermann, R. Engel and J. Ranft, *Phys. Rev.* **D49** (1994) 3236
- [60] T. Sjöstrand, *Comp. Phys. Comm.* **82** (1994) 74
- [61] S.Y. Shmakov, V.V. Uzhinski and A.M. Zadoroshny, *Comp. Phys. Comm.* **54** (1989) 125
- [62] A. Ferrari, J. Ranft, S. Roesler and P.R. Sala, *Z. Phys.* **C70** (1996) 413; *Z. Phys.* **C71** (1996) 75
- [63] G. Battistoni et al., *Nucl. Phys. B (Proc. Suppl.)* **52B** (1997) 120
- [64] D. Heck, internal report, unpublished (1997)
- [65] G. Schatz and D. Heck, in: Report **KfK 5027** (1992) 35, J. Knapp and H. Rebel eds., Kernforschungszentrum Karlsruhe
- [66] J.J. Gaimard, Thèse Université Paris 7 (1990); Report **GSI-90-27** (1990), Gesellschaft für Schwerionenforschung, Darmstadt
- [67] X. Campi and J. Hüfner, *Phys. Rev.* **C24** (1981) 2199
- [68] J.N. Capdevielle, *Proc. 23rd Int. Cosmic Ray Conf.*, Calgary, **4** (1993) 52
- [69] A. Dąbrowska et al., *Phys. Rev.* **D47** (1993) 1751
- [70] A.S. Goldhaber, *Phys. Lett.* **53B** (1974) 306
- [71] T.H. Burnett et al., JACEE Collaboration, *Phys. Rev.* **D35** (1987) 824
- [72] G. Barr et al., *Phys. Rev.* **D39** (1989) 3532
- [73] T. Kinoshita and A. Sirlin, *Phys. Rev.* **107** (1957) 593
- [74] C. Jarlskog, *Nucl. Phys.* **75** (1966) 659
- [75] D. Heck, internal report, unpublished (1993)
- [76] M. Aguilar-Benitez et al. (Particle Data Group), *Phys. Rev.* **D45** (1992) VII, 77
- [77] M. Aguilar-Benitez et al. (Particle Data Group), *Phys. Rev.* **D45** (1992) VII, 84
- [78] L. Jauneau, in: *Methods in Subnuclear Physics*, Vol. **III**, M. Nikolić ed. (Gordon & Breach, New York, 1969) 123
- [79] L.M. Chounet et al., *Phys. Rep.* **4** (1972) 199, App. 1

- [80] N. Cabibbo and A. Maksymowicz, *Phys. Lett.* **9** (1964) 352; *Phys. Lett.* **11** (1964) 360; *Phys. Lett.* **14** (1965) 72
- [81] M. Aguilar-Benitez et al. (Particle Data Group), *Phys. Rev.* **D45** (1992) VII, 6
- [82] J.G. Layter et al., *Phys. Rev. Lett.* **29** (1972) 316
- [83] Y.S. Tsai, *Rev. Mod. Phys.* **46** (1974) 815 and erratum *Rev. Mod. Phys.* **49** (1977) 421
- [84] T. Stanev et al., *Phys. Rev.* **D32** (1985) 1244
- [85] T. Ahmed et al., (H1 Collaboration), *Phys. Lett.* **B299** (1993) 374
- [86] M. Derrick et al., (ZEUS Collaboration), *Phys. Lett.* **B293** (1992) 465
- [87] A. Baldini et al., in: Landolt-Börnstein, New Series **I/12 a+b** (Springer, Berlin, 1987)
- [88] H. Genzel et al., in: Landolt-Börnstein, New Series **I/8** (Springer, Berlin, 1973)
- [89] R.M. Sternheimer et al., *Phys. Rev.* **B26** (1982) 6067
- [90] J. Spitzer, private communication (1988)
- [91] R. Attallah, private communication (1995)
- [92] R.L. Ford and W.R. Nelson, Report **SLAC 210** (1978), Stanford Linear Accelerator Center
- [93] L.D. Landau and I.Ya. Pomeranchuk, *Dokl. Akad. Nauk SSSR* **92** (1953) 535 & 735; A.B. Migdal, *Phys. Rev.* **103** (1956) 1811
- [94] K. Kasahara, Proc. Int. Symp. Extremely High Energy Cosmic Rays, Tanashi, Tokyo (Japan) (1996) 221
- [95] S. Sciutto, private communication (1997)
- [96] K. Greisen, in: Prog. Cosmic Ray Physics Vol. **III**, J.G. Wilson ed. (North Holland Publishing Co., Amsterdam 1965) 1
- [97] R.M. Barnett et al. (Particle Data Group), *Phys. Rev.* **D54** (1996) 1
- [98] K. Kamata and J. Nishimura, *Suppl. Progr. Theoret. Phys.* **6** (1958) 93
- [99] M.F. Bourdeau et al., *J. Phys. G: Nucl. Phys.* **6** (1980) 901
- [100] J. Nishimura, in: Handbuch der Physik, Vol. **XLVI/2**, S. Flügge ed. (Springer, Berlin, 1967) 1

- [101] F. Arqueros, S. Martinez and M. Rozanska, *Proc. 23rd Int. Cosmic Ray Conf.*, Calgary, **4** (1993) 738; S. Martinez et al., *Nucl. Instr. Meth.* **A357** (1995) 567
- [102] Handbook of Chemistry and Physics, 67th Edition, R.C. Weast ed. (The Chemical Rubber Co., Cleveland, 1986) E373
- [103] J.N. Capdevielle, *J. Phys. G: Nucl. Part. Phys.* **16** (1990) 1539
- [104] G.J. Alner et al., UA5 Collaboration, *Phys. Lett.* **B167** (1986) 476
- [105] R.E. Ansorge et al., UA5 Collaboration, *Z. Phys.* **C43** (1989) 75
- [106] G.J. Alner et al., UA5 Collaboration, *Nucl. Phys.* **B291** (1987) 445
- [107] J.N. Capdevielle and S. Zardan, *Proc. 20th Int. Cosmic Ray Conf.*, Moscow, **5** (1987) 160
- [108] K. Alpgård et al., UA5 Collaboration, *Phys. Lett.* **B115** (1982) 71; G. Arnison et al., UA1 Collaboration, *Phys. Lett.* **B122** (1983) 189; G.J. Alner et al., UA5 Collaboration, *Phys. Lett.* **B180** (1986) 415
- [109] R.E. Ansorge et al., UA5 Collaboration, *Nucl. Phys.* **B328** (1989) 36
- [110] T. Åkesson et al., AFS Collaboration, *Phys. Lett.* **B178** (1986) 447
- [111] C. Geich-Gimbel, *Int. J. Mod. Phys.* **4** (1989) 1527
- [112] A. Klar and J. Hüfner, *Phys. Rev.* **D31** (1985) 491
- [113] C. De Marzo et al., *Phys. Rev.* **D26** (1982) 1019
- [114] M. Arneodo et al., *Z. Phys.* **C31** (1986) 1
- [115] R. Attallah et al., *Proc. 23rd Int. Cosmic Ray Conf.*, Calgary, **4** (1993) 48
- [116] J.N. Capdevielle, *Proc. 5th Int. Symp. on Very High Energy Cosmic Ray Interactions*, Lodz, (1987) 1
- [117] M. Aguilar-Benitez et al., NA27 Collaboration, *Z. Phys.* **C50** (1991) 405
- [118] R. Attallah et al., *Proc. 22nd Int. Cosmic Ray Conf.*, Dublin, **4** (1991) 157
- [119] R. Hagedorn, *Rev. Nuovo Cim.* **6** (1983) 1
- [120] G. Arnison et al., UA1 Collaboration, *Phys. Lett.* **B118** (1982) 167
- [121] G. Bocquet et al., *Phys. Lett.* **B366** (1996) 434
- [122] J.N. Capdevielle, *Nucl. Phys. B (Proc. Suppl.)* **52B** (1997) 146

- [123] G.J. Alner et al., UA5 Collaboration, *Phys. Rep.* **154** (1987) 247
- [124] R. Attallah, private communication (1990)
- [125] J.A. Capella, *Proc. 22nd Int. Cosmic Ray Conf.*, Dublin, **5** (1991) 15
- [126] S. Jadach, *Comp. Phys. Comm.* **9** (1975) 297
- [127] J.N. Capdevielle and T. Thouw, *J. Phys. G: Nucl. Part. Phys.* **18** (1992) 143
- [128] D. Heck et al., *Proc. 23rd Int. Cosmic Ray Conf.*, Calgary **4** (1993) 60
- [129] R.E. Ansorge et al., UA5 Collaboration, *Z. Phys.* **C33** (1986) 175
- [130] P. Bernard et al., UA4 Collaboration, *Phys. Lett.* **B166** (1986) 459
- [131] V. Innocente et al., *Phys. Lett.* **B169** (1986) 285
- [132] J.N. Capdevielle and J. Gawin, *J. Phys. G: Nucl. Part. Phys.* **12** (1986) 465
- [133] G. Schatz, in: Report **KfK 5027** (1992) 32, J.Knapp and H.Rebel eds., Kernforschungszentrum Karlsruhe
- [134] A. Capella, Report **LPTHE 91/53** (1991), Orsay, France
- [135] T. Åkesson et al., HELIOS Collaboration, *Z. Phys.* **C49** (1991) 355

List of Tables

3.1	Computing times for various thinning levels	15
5.1	Basic features of the interaction models used	30
6.1	Decay modes and branching ratios for kaons	40
6.2	Coefficients of the parametrization of $K \rightarrow 3\pi$	41
6.3	Coefficients of the parametrization of $K \rightarrow \pi + \ell + \nu$	41
6.4	Decay modes and branching ratios for η	42
6.5	Decay modes and branching ratios for strange baryons	43
6.6	Decay modes and branching ratios for resonances	43
7.1	Branching ratios for photonuclear reactions leading to two pions . . .	50
7.2	Parameters of the longitudinal age formula	53
A.1	Parameters of the U.S. standard atmosphere	59
A.2	Parameters of the AT115 atmosphere (January 15, 1993)	59
A.3	Parameters of the AT223 atmosphere (February 23, 1993)	60
A.4	Parameters of the AT511 atmosphere (May 11, 1993)	60
A.5	Parameters of the AT616 atmosphere (June 16, 1993)	60
A.6	Parameters of the AT822 atmosphere (August 22, 1993)	61
A.7	Parameters of the AT1014 atmosphere (October 14, 1993)	61
A.8	Parameters of the AT1224 atmosphere (December 24, 1993)	61
A.9	Air pressure values at low altitude for various atmospheres	62
C.1	Parameters of the hadron-nucleon cross section parametrization . . .	66
D.1	Energy dependence of x_1 , x_2 , and α	74
D.2	Charge exchange of leading particles	75
D.3	Resonance formation of leading particles	76

List of Figures

2.1	Pressure difference of atmosphere relativ to U.S. standard atmosphere	7
3.1	Energy loss of muons as function of Lorentz factor	10
4.1	Inelastic proton-air cross sections at higher energies	20
4.2	Inelastic nucleon-air cross sections at lower energies	22
4.3	Inelastic hadron-proton cross sections	23
4.4	Inelastic nucleus-air cross sections	24
4.5	Inelastic hadron-air cross sections at higher energies	25
4.6	Inelastic meson-air cross sections at lower energies	26
7.1	Photoproduction cross section	49
B.1	Differences in muon range calculated with different approximations .	64